Water Resources Research

RESEARCH ARTICLE
10.1029/2018WR024431

Special Section:
Advances in remote sensing, measurement, and simulation of seasonal snow

Retrieval of Snow Water Equivalent, Liquid Water Content, and Snow Height of Dry and Wet Snow by Combining GPS Signal Attenuation and Time Delay

Franziska Koch[1,2], Patrick Henkel[3,4], Florian Appel[5], Lino Schmid[6], Heike Bach[5], Markus Lamm[4], Monika Prasch[2], Jürg Schweizer[6], and Wolfram Mauser[2]

[1]Institute of Hydrology and Water Management, University of Natural Resources and Life Sciences, Vienna, Austria, [2]Department of Geography, Ludwig-Maximilians-Universität München, Munich, Germany, [3]Institute for Communications and Navigation, Technical University of Munich, Munich, Germany, [4]Advanced Navigation Solutions GmbH, Munich, Germany, [5]VISTA Remote Sensing in Geosciences GmbH, Munich, Germany, [6]WSL Institute for Snow and Avalanche Research SLF, Davos, Switzerland

Abstract For numerous hydrological applications, information on snow water equivalent (SWE) and snow liquid water content (LWC) are fundamental. In situ data are much needed for the validation of model and remote sensing products; however, they are often scarce, invasive, expensive, or labor-intense. We developed a novel nondestructive approach based on Global Positioning System (GPS) signals to derive SWE, snow height (HS), and LWC simultaneously using one sensor setup only. We installed two low-cost GPS sensors at the high-alpine site Weissfluhjoch (Switzerland) and processed data for three entire winter seasons between October 2015 and July 2018. One antenna was mounted on a pole, being permanently snow-free; the other one was placed on the ground and hence seasonally covered by snow. While SWE can be derived by exploiting GPS carrier phases for dry-snow conditions, the GPS signals are increasingly delayed and attenuated under wet snow. Therefore, we combined carrier phase and signal strength information, dielectric models, and simple snow densification approaches to jointly derive SWE, HS, and LWC. The agreement with the validation measurements was very good, even for large values of SWE (>1,000 mm) and HS (> 3 m). Regarding SWE, the agreement (root-mean-square error (RMSE); coefficient of determination (R^2)) for dry snow (41 mm; 0.99) was very high and slightly better than for wet snow (73 mm; 0.93). Regarding HS, the agreement was even better and almost equally good for dry (0.13 m; 0.98) and wet snow (0.14 m; 0.95). The approach presented is suited to establish sensor networks that may improve the spatial and temporal resolution of snow data in remote areas.

Key Points:
- Snow water equivalent, liquid water content, and snow height were simultaneously derived with one sensor setup only
- This continuous and nondestructive approach for bulk snow cover properties determination is based on GPS signals travelling through snowpack
- The correlation with validation data for three entire winter seasons encompassing dry-snow accumulation and wet-snow melting periods is high

Supporting Information:
- Supporting Information S1

F. Koch and P. Henkel contributed equally.

Correspondence to:
F. Koch,
franziska.koch@boku.ac.at

Citation:
Koch, F., Henkel, P., Appel, F., Schmid, L., Bach, H., Lamm, M., et al. (2019). Retrieval of snow water equivalent, liquid water content, and snow height of dry and wet snow by combining GPS signal attenuation and time delay. *Water Resources Research*, *55*, 4465–4487. https://doi.org/10.1029/2018WR024431

Received 16 NOV 2018
Accepted 18 APR 2019
Accepted article online 2 MAY 2019
Published online 31 MAY 2019

1. Introduction

Snow is an essential climate variable contributing critically to the Earth's climate (World Meteorological Organization, 2018). Regarding hydrological aspects, snow is particularly important in mountainous regions, which are considered as the water towers of the adjacent lowlands (Viviroli et al., 2007). To this end, snow water equivalent (SWE) is the key variable to quantify the amount of snow and predict subsequent runoff (Jonas et al., 2009). Water from snowmelt is crucial for water resources management including fresh water supply, hydropower generation, irrigation, or navigation (Immerzeel et al., 2009; Mankin et al., 2015; Mauser & Prasch, 2015; Sturm, 2015; Wesemann et al., 2018). In situ snow measurements are fundamental for the evaluation and validation of various remote sensing products (e.g., Parajka & Blöschl, 2006; Takala et al., 2011) and snowpack models that consider, for example, snow accumulation and melting processes as well as lateral snow transport (e.g., Bernhardt et al., 2012; Frey & Holzman, 2015; Warscher et al., 2013; Weber et al., 2016; Vionnet et al., 2012). Moreover, they help improving model parameterizations for SWE estimation or reconstructions (e.g., Raleigh & Lundquist, 2012).

The snow cover properties SWE, snow height (HS), and snow wetness, mainly expressed as snow liquid water content (LWC), can be measured at different scales. This includes on the one hand various in situ and point scale measurements (Kinar & Pomeroy, 2015; Lundberg et al., 2010; Pirazzini et al., 2018), which may provide continuous data but cannot capture spatial variations. On the other hand, optical and microwave remote sensing applications (Dietz et al., 2012; Hall, 2012; Nagler et al., 2016; Tedesco, 2014) can

cover larger areas but might lack the desired temporal frequency or pixel resolution. Up to now, all methods have some limitations, which means that in many regions it is not always possible to determine all relevant snow cover properties. Hence, developing new and potentially low-cost measurement methods as well as establishing networks in mountainous catchments is much needed (Pirazzini et al., 2018; Pomeroy et al., 2015).

Regarding traditional in situ measurements, snow sampling techniques such as snow pit measurements are destructive, labor-intense, possibly error-prone, and infrequent (e.g., Goodison et al., 1987). Ground-based sensors for continuous SWE and HS measurements are still scarce in many regions. Automatic point-scale measurements of HS are mainly based on ultrasonic or laser depth sensor techniques (Pirazzini et al., 2018). Standard SWE measurement sensors such as snow pillows or scales are quite large and expensive, difficult to install, and are prone to measurement errors due to bridging effects within the snowpack (Beaumont, 1966; Johnson & Marks, 2004). SWE measurements based on terrestrial cosmic ray sensors show promising results (Schattan et al., 2017) but still face problems when the snow depth is large and/or the snow turns wet (Sigouin & Si, 2016). In situ measurements of LWC are even more scarce compared to HS and SWE measurements. Boyne and Fisk (1987) and Techel and Pielmeier (2011) provide a good overview on in situ LWC measurements. They are mainly based on hand-held dielectric devices, which are used in snow pits (Denoth, 1989; Sihvola & Tiuri, 1986). However, various sources of errors have been shown as their application is destructive. Schneebeli et al. (1998) and Avanzi et al. (2014) presented first results of continuous LWC measurements with time domain reflectometry and capacity probes, respectively. However, they reported that quantitative interpretation is challenging due to, for example, air pockets that easily form around the sensors. Nondestructive measurements of wet-snow or even LWC alongside with the determination of further snow cover properties were obtained with different radar systems (e.g., Bradford et al., 2009; Heilig et al., 2015; Lundberg & Thunehed, 2000; Mitterer et al., 2011; Schmid et al., 2014) but are rather expensive for operational application.

Satellite remote sensing is a good alternative to derive snow cover properties such as SWE, HS, or the onset of snow melt and has the advantage to provide information on their spatial distribution. However, for many regions or hydrological applications, such as hydropower production and flood forecasting, the spatial and/or temporal resolution is still insufficient. Optical remote sensing products often face no-data problems due to cloud cover. Active microwave products are prone to radar shadows caused by so-called layover or foreshortening effects, which result from relief displacements, especially in mountainous regions. Combinations of different sensors and techniques, in situ and remote sensing approaches, as employed in the National Aeronautics and Space Administration SnowEx campaign, seem very promising (Kim et al., 2017). More recent terrestrial or airborne techniques include, for example, laser scanning (Grünewald et al., 2010; Prokop, 2008) or digital photogrammetry (Bühler et al., 2016); both techniques provide snow depth with high spatial resolution. Yet these measurements only provide a snapshot in time and are not available in all alpine and remote areas. An alternative approach with low-cost cameras or webcams was presented by Härer et al. (2018).

In the last decade, several approaches based on L-band Global Navigation Satellite (GNSS) signals were developed to derive snow cover properties. GNSS encompasses several satellite systems like the U.S. Global Navigation Satellite System (Global Positioning System [GPS]), the European Galileo system, the Russian GLONASS system, and the Chinese Beidou system. The majority of these approaches employ reflectometry techniques by using permanently installed, mainly high-end geodetic antennas. They derive HS by exploiting signals that were reflected at the air-snow interface (Larson et al., 2009). Gutmann et al. (2012) evaluated this technique successfully for an entire winter season. Boniface et al. (2015) and Larson (2016) used networks of geodetic stations to derive HS around the stations at numerous locations in the western U.S. Botteron et al. (2013); Cardellach et al. (2011) and Jin et al. (2014) give an overview on several GNSS reflectometry approaches. Even though obstacles might influence the measurements, Vey et al. (2016) reported that this technique might also be applicable for urban areas. Completely different GNSS approaches were shown by Stepanek and Claypool (1997) and Schleppe and Lachapelle (2008), who observed the signal reception and tracking performance of low-cost GPS receivers under a snow avalanche deposit. Koch et al. (2014) used GPS signal strength attenuation of buried antennas to continuously and nondestructively derive LWC. Steiner et al. (2018) theoretically and practically investigated the behavior of GPS signals of submerged antennas. By exploiting the GNSS carrier phases using low-cost sensors, Henkel et al. (2018) derived SWE for

dry-snow conditions. Steiner et al. (2018) confirmed the applicability applying a similar approach but using geodetic sensors and calculated daily SWE values for an entire winter season applying different ambiguity resolution strategies and using widelane combinations. SWE values were represented fairly well; however, no distinction between dry- and wet-snow conditions was made. This might lead to potential overestimations or underestimations depending on LWC. With the above mentioned GNSS-based approaches, mainly one snow cover property was determined at a time.

Our aim is therefore to derive with one single measurement setup the snow cover properties SWE, HS, and snow LWC. To this end, we will combine our previous analyses based on GPS L1-band carrier phases and signal strengths. In Koch et al. (2014), we used GPS signal attenuation to derive LWC and in Henkel et al. (2018), we derived SWE based on GPS carrier phase measurements expressing the time delay in snow. For the first method, however, HS was still needed as an external input to derive bulk volumetric LWC, and for the second approach, we were able to derive SWE reliably only for dry-snow conditions. In Schmid et al. (2015), we combined GPS signal attenuation with L-band travel time information in snow recorded with an upward-looking ground-penetrating radar. The good results of this sensor combination, using information on time delay and signal attenuation, encouraged us to develop a similar approach by solely using GPS signals, as already had been suggested by Koch (2017) and Henkel et al. (2017).

2. Study Site and GPS Sensor Setup

2.1. Study Site and Accompanying Data

The study was performed at the high-alpine site Weissfluhjoch (46°49′47″N, 9°48′34″E, 2,536 m above sea level), near Davos in Switzerland. The flat study site is operated by the WSL Institute for Snow and Avalanche Research SLF and is snow-covered during almost two thirds of the entire year. The site is well equipped with numerous sensors recording continuously meteorological and snow cover properties (Marty & Meister, 2012). It has power supply and internet access. As various reference measurements are available for validation, it is an ideal location for testing and developing new snow measurement sensors.

An overview of the locations of the applied sensors and manual measurements is given in Figure 1. For the validation of the GPS-derived snow cover properties, we used continuously measured SWE and offset-corrected data from a snow pillow and a snow scale by setting the recordings to zero in autumn. HS was recorded continuously with two ultrasonic sensors (Ultrasonic 1 and 2) and was measured manually once a day at approximately 8 a.m. at a snow stake. Moreover, we used air and snow surface temperature data, which were recorded at the location of Ultrasonic 2, as well as data from a 5-m^2 snow lysimeter, measuring the meltwater discharge at the bottom of the snowpack. Furthermore, we used information from snow pit measurements (Marty, 2017), taken weekly or biweekly, which were performed according to Fierz et al. (2009). The snow profiles were dug along three profile lines. From the snow profiles, we used bulk SWE, HS, and snow density. Snow density was determined by weighing snow samples of known volumes. The snow pit SWE data are denoted as Manual 1. As snow density is spatially less variable than SWE or HS (Jonas et al., 2009), we multiplied the snow pit density with the snow depth recorded at the snow stake to obtain additional bulk SWE values (Manual 2). The snow stake recordings were denoted as Manual 3 and HS measured in the snow pits as Manual 4. All sensors as well as the snow profile lines and the snow stake are located close by with distances of 5 to 25 m between each other (Schmid et al., 2015).

Our study covers the three snow-covered seasons 2015-2016, 2016-2017, and 2017-2018. To ease comparison with the manual snow pit and snow stake measurements, we needed validation data at a daily resolution. Hence, we referred all validation measurements to 8 a.m., when the manual measurements usually took place. For the continuous SWE, HS, and temperature measurements, we used the corresponding measured values at 8 a.m. For the meltwater outflow at the lysimeter we calculated a 24-hr average between 8 p.m. of the previous day and 8 p.m. of the actual day. Due to a recording failure, data of the snow pillow, snow scale, and snow lysimeter were lacking between 3 and 17 February 2017. Also, no data were available for the snow scale from 30 May 2017 until the end of this season due to a sensor failure. Otherwise, the SWE validation data are complete for the entire three snow-covered seasons. Regarding the continuous HS data, Ultrasonic 2 and snow stake measurements are complete for all three seasons; Ultrasonic 1 data are available for 2015-2016 and 2017-2018. The snow surface temperature was recorded since 18 March 2016.

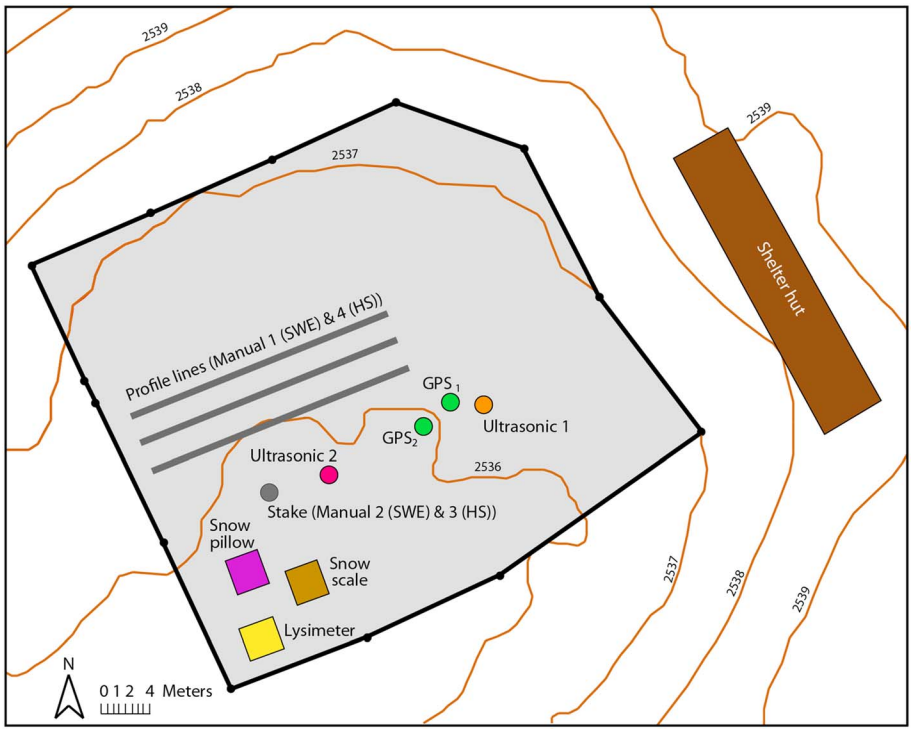

Figure 1. Overview of the study site Weissfluhjoch (WFJ) above Davos (Switzerland) showing the locations of the various sensors including GPS_1 and GPS_2, the manual snow depth observation at the stake, and the area of the three snow profile lines for manual snow pits at. Internet and energy supply were provided at the sheltered hut. The elevation contour lines are given in meters.

2.2. GPS Data and Sensor Setup

The sensor setup is composed of two static GPS antennas. One antenna (GPS_1) was mounted on the top of a pole, and the other one (GPS_2) was placed on the ground. Figure 2a gives a schematic overview including the exemplary pathways of one GPS satellite at a specific elevation angle during one observation time step. Figure 2b shows the approximately 5-m high poles and racks, which were used at the test site Weissfluhjoch and the locations of GPS_1 and GPS_2. During the snow-covered season, GPS_2 was covered with snow such that the received GPS signals were influenced by travelling through the snowpack, whereas GPS_1 was permanently above the snow cover since the maximum HS at Weissfluhjoch did not exceed 5 m. This setup is similar to the ones previously described (Henkel et al., 2018; Koch et al., 2014). The GPS sensors were installed on 10 October 2015, and the data are still recorded. GPS raw data were recorded for the three entire snow-covered seasons corresponding to the three winter seasons of 2015-2016, 2016-2017, and 2017-2018. The data set is complete, except for 2 days (21 and 22 June 2016) when data are missing due to a power failure. The GPS data were processed for time windows of 24 hr to allow a daily resolution of the GPS-derived bulk snow cover properties, as an average over this time window, as this temporal resolution often is used for hydrological studies. The corresponding time step of the daily average was set to 8 a.m. to conform to the manual snow measurements. For this reason, we started the snow processing of the 24-hr time window at 8 p.m. for each day and stopped it at 8 p.m. at the following day.

We used two low-cost u-blox LEA-6T GPS receivers, which were connected to a small single board PC including a data logger. The receivers were connected via 5-m coax cables with commercially available, active low-cost u-blox patch antennas (type: ANM-MS-0) with 29-dB gain. The receiver of GPS_1 was stored in a small box on the pole. The receiver of GPS_2 and the PC were stored in a weather-proofed box on the ground of the study site next to the pole. The PC was connected to the energy and internet supply in the sheltered hut (see Figure 1). On the ground we protected all cables to avoid animal bites during summer time. The size of the antennas is small, approximately 3.5 cm × 3.5 cm; they were each additionally fixed on a 5-cm × 5-cm ground plane. This setup minimizes the reception of reflections from

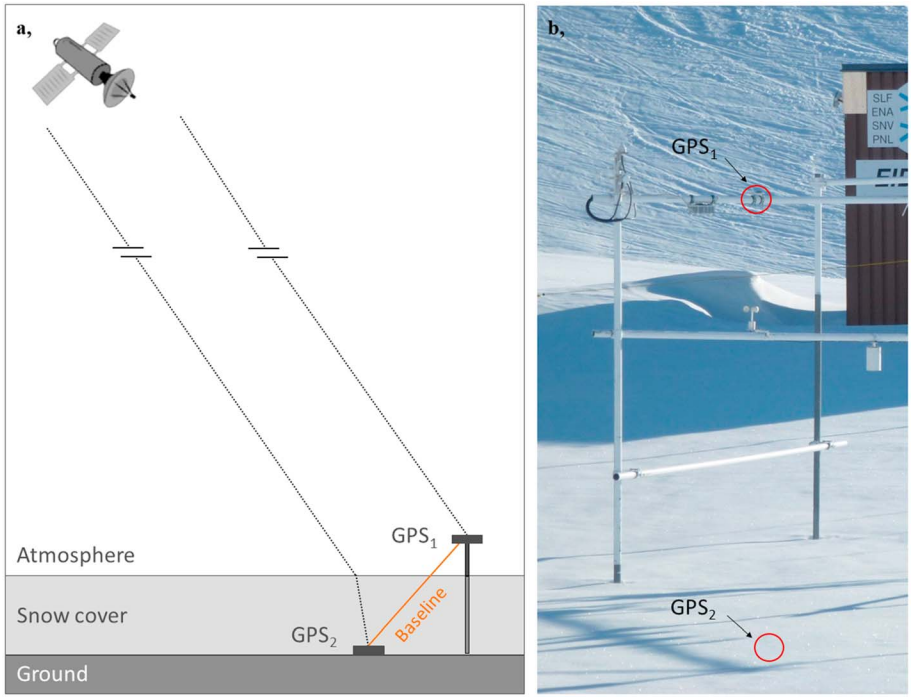

Figure 2. (a) Schematic Global Positioning System (GPS) setup for the derivation of snow cover properties including the baseline between the ground and pole antenna. Exemplarily, the signal paths of one GPS satellite to the two antennas are shown. The paths can be assumed to be parallel since the distance between both ground antennas is much smaller than the distance to the satellite. (b) Locations of the GPS_1- and GPS_2 antennas at the test site Weissfluhjoch. The photo was taken at a date with a snow height of approximately 2 m above GPS_2.

below, which is especially relevant for the upper antenna. We tried to keep the surface area small to avoid snow accumulation on top of the upper antenna GPS_1. In fact, the upper antenna was snow-free most of the time as confirmed by webcam observations. After a snowfall, a few millimeters might have accumulated on top of the GPS_1 antenna, but the wind removed the snow quickly, so that we could reasonably neglect potential snow accumulation on the upper antenna. In general, the study site Weissfluhjoch is ideal for GPS signal reception in mountainous regions. The GPS satellite coverage is very high due to almost unobscured sky visibility above 10° elevation in the southern directions and slightly above approximately 15 to 20° elevation in all other directions (Steiner, Meindl, Fierz, & Geiger, 2018). For this reason and because signals from very low elevation angles are quite weak and prone to multipath effects, which means that the reception of a specific GPS signals is influenced by multiple signal paths due to reflections on the Earth's surface, we applied a 15° elevation mask for all azimuth directions. Consequently, we eliminated the GPS pseudorange and carrier phase measurements from any satellite below this mask.

Theoretically, all GNSS signals, including signals from GPS, Galileo, Glonass, and Beidou, could be used for this approach. However, to be able to apply a low-cost sensor system with well-known simple patch antennas and standard positioning chips, we used the freely available GPS L1-band signals at 1.57542 GHz. The wavelengths of the GPS signals are in comparison to the size of snow grains significantly smaller with approximately 1 mm (Fierz et al., 2009). The effect of a potential interaction of snow microstructure and surface roughness with GPS signals was neglected in this study but will be subject of further studies. Moreover, as we cannot discriminate internal snow layers, we assume the entire snowpack as one single layer with bulk properties as shown schematically in Figure 2a. In addition, we neglect potential pseudorange multipath effects as we use carrier phase measurements for the SWE determination, which are by orders of magnitude less influenced by multipath effects than pseudorange measurements. For the derivation of signal strength attenuation, this neglection is also applicable as mentioned in Koch et al. (2014). For the combined derivation of SWE, HS, and LWC, we used carrier phase and signal strength information from each visible GPS satellite above the 15-degree mask for each time step of

observation. The term signal strength was set equal to the recorded carrier-to-noise power density ratio C/N_0 within this study. The GPS data were tracked at a temporal resolution of 1 s, and we made use of the signals from all available 32 GPS satellites, which passed over the test site for several hours each sidereal day. If one of the 32 GPS satellites was temporarily flagged unhealthy, we excluded the data of the respective GPS satellite in our calculations. After applying the elevation mask, it was possible to use up to 10 satellites for processing in parallel for each time step.

3. Theory: Influences of Snow on GPS Signals

3.1. Dielectric Properties of Dry and Wet Snow

Each material has specific dielectric properties, which depend on the frequency of the incident electromagnetic waves. The response of a dielectric material to an applied electromagnetic field is not instantaneous and leads, if not in vacuum, to a phase difference and amplitude decline (Woodhouse, 2005). The dielectric permittivity of a certain medium like snow is defined as the product of the vacuum permittivity ε_0 and the relative dielectric permittivity ε. The latter is medium-specific and is considered complex

$$\varepsilon = \varepsilon' + i\varepsilon'' \tag{1}$$

The real part ε' is related to the stored energy; the imaginary part ε'' is related to the loss of energy within a medium and is also called dielectric loss factor (Ulaby et al., 2014). GPS L1-band signals are electromagnetic waves, which are broadcast in the L-band microwave domain at a carrier frequency of 1.57542 GHz with a wavelength of approximately 19 cm. In the microwave range the interactions between the electromagnetic waves and a certain material are expressed as dipolar processes describing the rotation and vibration of polar molecules. As long as GPS signals travel through space and atmosphere, they are less affected compared to the attenuation effects, which occur as soon as they come upon the Earth's surface or travel through media like snow. Depending on the dielectric properties of snow, the GPS signals are affected by signal attenuation, time delay, and reflection and refraction (Woodhouse, 2005).

Dry snow is a mixture of air and ice, whereas wet snow is a three-phase mixture composed of air, ice, and liquid water. Comparing the influences of dry and wet snow, the latter significantly affects the signals due to the presence of liquid water. Water has, compared to the other components, very prominent dielectric properties. As the dielectric properties of dry and wet snow are composed of the dielectric properties of air, ice, and water, it is obvious that the dielectric properties of wet snow are markedly different of those of dry snow. The permittivity of dry and wet snow might be either estimated empirically (e.g., Denoth, 1989; Sihvola & Tiuri, 1986) or by three-phase mixing models (e.g., Lundberg & Thunehed, 2000; Roth et al., 1990). Most dielectric snow models are valid for a LWC up to 8% by volume (Bradford et al., 2009), being also the maximum range, or even lower, which is usually observed in an alpine seasonal snowpack (Heilig et al., 2015). In the microwave L-band domain, the real part of dry snow is approximately 1.7 (Schmid et al., 2014), which might, however, slightly vary depending on the density of the snowpack (Tiuri et al., 1984). The imaginary part of dry snow can be neglected as the imaginary parts of air and ice are both approximately 0. Regarding wet snow, the real part ranges between 1.7 and 4.0, depending on the LWC (0-8%) and the applied dielectric model (Koch et al., 2014). In contrast to dry snow, the imaginary part of wet snow cannot be neglected and ranges between 0 and 0.3 for a LWC up to 8% (Tiuri et al., 1984). Following Schmid et al. (2015), we applied the dielectric three-phase mixing model after Roth et al. (1990) defining the real part of the complex permittivity of snow ε'_s as

$$\varepsilon'_s = 0.01\ \mathrm{LWC}\ \sqrt{\varepsilon'_w} + \frac{\rho_{s,d}}{\rho_i}\sqrt{\varepsilon'_i} + 1 - \frac{\rho_{s,d}}{\rho_i} - 0.01\ \mathrm{LWC}\sqrt{\varepsilon'^{2}_a} \tag{2}$$

with the real parts of the permittivity of air ε'_a, ice ε'_i, and water ε'_w as listed in Table S1 in the supporting information, the density of ice ρ_i=917 kg/m^3 and an assumption for the dry snow density $\rho_{s,d}$=357 kg/m^3, which is an estimate of the average maximum dry snow density at the study site Weissfluhjoch (Schmid et al., 2015). The frequency-dependent imaginary part of snow was calculated with the semiempirical equation after Tiuri et al. (1984) by

$$\varepsilon_s'' = \frac{f}{10^9 \mathrm{Hz}} \left(1.0{\times}10^{-3}\ \mathrm{LWC} + 8.0{\times}10^{-5}\ \mathrm{LWC}^2\right) \varepsilon_w'' \tag{3}$$

with the imaginary part of water ε_w'' as listed in Table S1 and the GPS L1-band frequency f=1.57542 GHz. LWC is given in percent per volume.

3.2. Signal Propagation in Snow

The dielectric properties of snow have a direct influence on GPS signal propagation, encompassing signal speed, refraction, reflection, and attenuation. In particular, as soon as liquid water is present, the change in signal propagation in snow is pronounced. The main effects are summarized in the following: for more details on the calculation of GPS signal attenuation, reflection, and refraction as well as signal power losses related to snow, we refer the reader to Koch et al. (2014) and Steiner, Meindl, and Geiger (2018).

The phase velocity of electromagnetic waves, being the speed of signals, can be derived after Maxwell's equations. For a low-loss dielectric material such as snow, the phase velocity v_s within the nonmagnetic material snow can be simplified (Bradford et al., 2009) to

$$v_s = \frac{c_0}{\sqrt{\varepsilon_s'}} \tag{4}$$

where c_0 is the speed of light in vacuum. If the signals travel through another medium than vacuum or air, the signal speed decreases, which is expressed as propagation time delay. Inserting Eq. (2) in Eq. (4), the speed of signals in snow v_s can be calculated. The speed of L-band microwaves travelling through dry snow is approximately 2.3×10^8 m/s after Schmid et al. (2014). Regarding wet snow, the propagation delay increases markedly as the signal speed decreases depending on the LWC.

GPS signals arrive at the Earth's surface at oblique angles. At medium boundaries like the air-snow interface, GPS signals are partly reflected and refracted following Snell's law. The angle of incidence in air θ_a, which is the elevation angle of a GPS satellite at a certain time step, and the corresponding angle of refraction in snow θ_s, which depends on the dielectric properties of snow, are related to the refraction coefficients of air n_a and snow n_s and the signal speeds in air $v_a \cong c_0$ and in snow v_s by

$$\frac{n_a}{n_s} = \frac{\sin\theta_s}{\sin\theta_a} = \frac{v_s}{v_a} \tag{5}$$

The refraction index is defined as the square-root of the relative dielectric permittivity, which depends on the LWC in snow. The refractive angle of air is 1 and is approximately 1.3 for dry snow. Regarding wet snow, the refractive index depends largely on LWC and reaches approximately 2 at 8% LWC. Depending on the refractive index, the geometrical path length d_s in snow is related to a theoretical not refracted path length d_a given in meters in air by

$$d_s = \frac{d_a}{\cos\theta_s} \tag{6}$$

The refraction angle and the path length change as well as the considered area of the investigated medium change depending on the wetness of the medium. This was exemplarily shown for different soil moisture values in Koch et al. (2016). As the angle of refraction decreases with increasing LWC, the geometrical path length of the GPS signals in snow decreases as well. The incident, reflected, and transmitted signals follow the Fresnel equations of reflection and transmission and the law of conservation of power (Woodhouse, 2005). The mean reflected power P_r consists of a real and an imaginary part of the complex circular reflection coefficients with co- and cross-polarized components (Steiner, Meindl, & Geiger, 2018). These components are used to describe the linear horizontal and vertical reflection coefficients, r_h and r_v, which are related to the complex permittivity of snow as well as the incident and refracted angles in snow. The detailed calculation of the reflection angles, coefficients, and the reflected power is described in Koch et al. (2014) and Steiner, Meindl, and Geiger (2018). Hence, the reflected power P_r is given by

$$P_r = \frac{r_h^2 + r_v^2}{2} \tag{7}$$

By travelling through a medium like snow, the GPS signal power decreases, which is described as signal attenuation. The power P_t, which is incidentally transmitted into snow, declines to the attenuated power P_a after passing through the snowpack for a certain path length d_s by following the exponential Beer-Lambert law (Ulaby et al., 2014)

$$P_a = P_t \exp(-\kappa d_s) \tag{8}$$

The attenuation coefficient κ for the GPS L1-band frequency f is defined as

$$\kappa = \sqrt{\frac{\mu_0}{\varepsilon_s' \varepsilon_0}}\ \varepsilon_s'' \varepsilon_0 2\pi f \tag{9}$$

with μ_0 being the vacuum permeability and ε_0 the vacuum permittivity. Equation (9) is valid for $\varepsilon''/\varepsilon' < 0.1$, which is the case for both, dry and wet snow (Ulaby et al., 2014; Woodhouse, 2005). The attenuation in dry snow is almost negligible, as also the imaginary part of dry snow is negligible, whereas the attenuation in wet snow increases with increasing LWC. The penetration depth is the reciprocal of the attenuation coefficient and is defined as the depth at which the signal power decreases to 1/e (~37%) of its incident value (Ulaby et al., 2014). For dry snow, the penetration depth reaches hundreds of meters but is reduced markedly for wet snow to the (sub)meter level (Mätzler, 2002). It is still possible to track GPS signals below wet snow continuously. However, the likelihood for signal interruptions increases for large values of SWE combined with high values of LWC.

4. Determination of Snow Cover Properties

4.1. Snow Water Equivalent

The derivation of SWE is based on the model for differential GPS carrier phase measurements as described in Henkel et al. (2018). It corresponds to the model used for real-time kinematic (RTK) positioning with an additional term for the snow-induced time delay. As the GPS pseudorange measurements are too noisy for SWE derivation, we only use GPS carrier phase measurements φ, which we took as an output of the receiver's raw data protocol. To eliminate receiver and satellite clock offsets, phase biases, and to mitigate atmospheric errors, the carrier phase measurements were combined in double differences (DDs) for the not co-located antenna pair {1, 2} of GPS_1 and GPS_2 (see Figure 2) and any satellite k and common reference satellite l as

$$\begin{aligned} \lambda\, \varphi_{12}^{kl} &= \lambda\left(\varphi_1^k - \varphi_2^k\right) - \left(\varphi_1^l - \varphi_2^l\right) \\ &= \overrightarrow{e}^{kl}\overrightarrow{b}_{12} + c_{12}^{kl} + \lambda N_{12}^{kl} + \frac{\lambda}{2}\Delta N_{12}^{kl} + \frac{c_0}{v_s} m^{kl}\mathrm{SWE} + \lambda\, \Delta\varphi_{\mathrm{MP},12}^{kl} + \epsilon_{12}^{kl} \end{aligned} \tag{10}$$

with the wavelength λ, the baseline vector $\overrightarrow{b}_{12}$ between GPS_1 and GPS_2, which is multiplied by the satellite-satellite difference of the normalized line-of-sight vectors $\overrightarrow{e}^{kl}$, the synchronization correction c_{12}^{kl}, the integer ambiguities N_{12}^{kl} due to the periodicity of the carrier phases, the half-cycle slip $1/2\ \Delta N_{12}^{kl}$, the snow-related term $c_0/v_s\ m^{kl}$ SWE, including the speed of light in vacuum c_0 and in snow v_s, the differential mapping function m^{kl} and SWE, the phase multipath $\Delta\varphi_{\mathrm{MP},12}^{kl}$, and the phase noise ϵ_{12}^{kl}. Besides the snow-related term, all other variables are part of standard RTK positioning algorithms, described, for example, in Talbot (1993), Teunissen (1995a, 1995b), Henkel and Cárdenas (2014), and Henkel et al. (2016).

The baseline vector $\overrightarrow{b}_{12}$ was derived for snow-free conditions using RTK positioning, which is, however, using both GPS carrier phase measurements φ_{12}^{kl} and GPS pseudorange measurements ρ_{12}^{kl}. The baseline determination has to be very accurate, as, for example, an error of 2.5 cm would already cause an error in SWE of 50 mm (Henkel et al., 2018). Consequently, the anchoring to the ground of the mast for the upper antenna has to be stable to prevent tilting and sinking. Thus, an RTK fixed solution is definitely required. Knowing $\overrightarrow{b}_{12}$ from the snow-free reference and considering the synchronization correction c_{12}^{kl}, it is

possible to jointly estimate SWE and the carrier phase ambiguities (Henkel et al., 2018) with an integer least squares estimator (Teunissen, 1995b). The errors of the phase multipath and the phase noise are unknown but in combination typically less than 2 cm. The fixed carrier phase integer ambiguities and the baseline are subtracted from the DD carrier phase measurements. The obtained terms are called carrier phase residuals. They depend on the snow-related term, the phase noise and multipath. Without snow cover, the residuals would be close to zero, showing only the effects of phase multipath and the phase noise.

However, with snow cover on top of GPS_2, the carrier phase residuals are mainly dependent on the respective GPS satellite elevation angle and increase in height with an increase in SWE. An example of DD carrier phase residuals largely influenced by snow is presented in Henkel et al. (2018) and additionally shown in Figure S1 in the supporting information. The raw DD carrier phase residuals follow an arc-formed shape in the presence of snow, but as they are affected by phase noise and multipath, the raw residuals show no smooth line. We additionally fitted the residuals with fixed residual arcs derived from a least-square estimation of the raw residuals to eliminate these deviations. For details on the specific modeling of the fixing of initial integer ambiguities, the initialization of the ambiguities of newly tracked satellites, the re-adjustment of ambiguities, the determination of fixed phase residuals, and calculated fitted fixed arcs, we refer to the detailed description in Henkel et al. (2018).

Regarding the snow-related term in Eq. (10), the speed of the GPS signals in snow and the mapping function have to be known. The mapping function is defined as the ratio between the slant delay of each GPS signal through the snowpack, and it depends on the elevation of the refracted signal recorded at the GPS receiver below the snowpack. Therefore, the GPS satellite elevation angles have to be converted to refracted angles to be conform with the geometrical path length in snow. For dry snow, $v_{s,d}$ and the refraction index $n_{s,d}$, which are both closely related to its dielectric properties, are assumed to be similar in comparison to the rather large differences in wet snow (Schmid et al., 2014; Tiuri et al., 1984). We applied $v_{s,d} = 2.3 \times 10^8$ m/s after Schmid et al. (2014) and assumed $n_{s,d} = 1.3$ for dry snow. For wet snow, however, it is not possible to just rely on carrier phase measurements. As shown in Koch et al. (2014), LWC can be derived by combining signal strength information and HS. The refractive index and the speed of the GPS signals for wet snow largely depend on LWC, which is related to the real and imaginary part of the complex permittivity of snow as shown in Eq. (2) and (3). Combining Eq. 2 with Eq. (4), the signal speed in wet snow is expressed as

$$v_s = \frac{c_0}{0.01\ \mathrm{LWC}\ \sqrt{\varepsilon'_w} + \frac{\rho_{s,d}}{\rho_i}\sqrt{\varepsilon'_i} + \left(1 - \frac{\rho_{s,d}}{\rho_i} - 0.01\ \mathrm{LWC}\right)\sqrt{\varepsilon'_a}} \tag{11}$$

The refractive index of wet snow $n_{s,w}$ is retrievable by using Eq. (5) to correctly calculate the geometrical path length in snow and is a necessary input for the mapping function m^{kl}.

4.2. Liquid Water Content in Snow

During the snow-covered period, the snow-influenced normalized GPS signal strength $P_{m,s}$ was continuously measured at GPS_2. The determination of a normalized signal strength was carried out after Koch et al. (2014) and Schmid et al. (2015). The recorded signal strengths depend mainly on the elevation angle of each GPS satellite passing by, as presented, for example, in Lighari et al. (2017). Considering low-cost GPS antennas, the recorded signal strengths depend also on the azimuth angle, as the antenna sensitivity pattern is likely to be azimuth angle-dependent. Moreover, the peak field strength of each GPS satellite might vary slightly due to the satellite series, aging, or other characteristics (Hofmann-Wellenhof et al., 2007). The snow-influenced signal strength values $P_{m,s}$ were recorded for each satellite at a specific elevation and azimuth angle for each time step. For the LWC derivation, these values were then related to a snow-free reference signal strength $P_{m,ref}$, which was also recorded at GPS_2. The reference values were stored in a three-dimensional matrix suggested in Koch et al., 2014 with 15 elevation classes in 5-degree steps between 15 and 90°, and 16 azimuth classes in 22.5-degree classes for all azimuth directions for each of the 32 GPS satellites.

Following the GPS signal strength loss model of Koch et al. (2014), the known signal strengths of $P_{m,s}$ and $P_{m,ref}$ can be related to the transmitted P_t and the attenuated signal strength P_a or the reflected P_r and attenuated signal strength P_a, by

$$P_{m,s} = P_t - P_a = P_{m,ref} - P_r - P_a \quad (12)$$

Regarding dry snow, the signal strength losses are small. As shown in section 3.2 the attenuation is almost negligible for dry snow and the losses are mainly attributed to reflection. Therefore, the signal strengths recorded beneath dry snow stays more or less constant, even if the amount of snow changes. For wet snow, however, the signal strength losses increase significantly with signal attenuation. As the complex permittivity of snow is related to P_t, P_a and P_r, they can be described with the dielectric models (Eq. (2) and (3)). Although the complex permittivity of wet snow is unknown, LWC can finally be obtained with a root-finding function considering all equations described in section 3 for attenuation, reflection, and refraction, provided HS is known. For further details we refer to Koch et al. (2014). Figure S2a in the supporting information demonstrates the exponential impact of LWC on the signal strength applying Eq. (12). However, information on HS is still missing, which is needed to describe the bulk LWC as a volumetric measure.

4.3. Snow Height

In general, HS and SWE are related by the density ρ_s of snow by

$$HS = \frac{SWE}{\rho_s} \quad (13)$$

However, it is not straightforward to correctly estimate ρ_s for the conversion of SWE to HS or vice versa. Jonas et al. (2009), McCreight et al. (2014), and Sturm et al. (2010) presented estimation approaches for bulk snow density based on seasonality, snow depth, site elevation, and location. Bormann et al. (2013) described the dominant climatological drivers for snow densification rates. Physically based snowpack models often apply even more complex parametrizations including several variables such as air temperature, relative humidity, and wind speed to derive the initial snow density. Subsequently, densification depends on settling and snow metamorphism (e.g., Lehning et al., 2002; Vionnet et al., 2012). For this study, however, we restrict ourselves to GPS data and site-specific information from former studies (e.g., Heilig et al., 2015; Mitterer et al., 2011; Schmid et al., 2014) to be independent of other measurements such as air temperature. By doing so, we are aware that some physical processes affecting densification are not adequately captured, which may lead to errors in our HS estimates. These deviations might occur in particular during rain-on-snow events or periods of warm weather, especially at lower elevations, which we will investigate in more detail in the future. The parameterization of snow densification at high-alpine sites is assumed to be more straightforward. Moreover, regarding SWE and snow density over a given area, the former is likely to considerably vary in space, whereas the latter is less affected by spatial variability (Jonas et al., 2009). This means that errors in snow density have in general a smaller effect on the calculation of HS than errors in SWE.

For this approach, the calculation of HS includes separate assumptions for dry- and wet-snow conditions. In case of dry-snow, HS is calculated based on a time-dependent snow densification approach considering changes in SWE over all former time steps as shown in section 5.3.2, whereas in case of wet-snow, HS is calculated iteratively from SWE and LWC including also information of the previous time step as described in section 5.3.3. In the following, we shortly describe how HS is calculated under dry- as well as wet-snow conditions.

Regarding a wet snowpack, snow layers become increasingly less distinct with ongoing wetting than they were under dry-snow conditions as wet snow metamorphism tends to make the snowpack more uniform. Therefore, we applied a bulk density approach, which was already applied by Schmid et al. (2015). We calculated HS from SWE and the wet snow density $\rho_{s,w}$

$$HS = \frac{SWE}{\rho_{s,w}} = \frac{SWE}{\rho_{s,d,max} + a\,LWC\,\rho_w} \quad (14)$$

where $\rho_{s,w}$ is approximated by $\rho_{s,d,max}$=357 kg/m^3, the density of water ρ_w=1,000 kg/m^3, and LWC and the factor a=3.08. The values used for a and $\rho_{s,d,max}$ were derived in former studies conducted at the study site Weissfluhjoch; the factor a had been introduced to counteract the underestimation of snow density resulting from the assumption that $\rho_{s,d,max}$ stays constant throughout the melt season (Schmid et al., 2014). To eliminate errors at times with large values of LWC, the maximum wet-snow density $\rho_{s,w}$ was limited to 600 kg/m^3.

Under dry snow conditions, we consider a time-dependent densification of the snowpack. A dry snowpack typically consists of multiple snow layers with potentially different snow densities due to different age since deposition. We assume that the density of a bulk dry snowpack follows in general a nonlinear evolution. López-Moreno et al. (2009) suggested an exponential behavior of bulk snowpack densification, which we follow in principle, but for each layer separately. In our dry snow densification model, we assume for each considered time window j (e.g., one day) that newly added SWE, represented as $\Delta\mathrm{SWE}_j$, is added on top of the snowpack. For time windows with no precipitation, $\Delta\mathrm{SWE}_j$ is set to zero. As we start our measurements for each winter season in autumn during the snow-free period, we assume that SWE of the time step before the first measurement, which corresponds to SWE(0), is 0 mm. Per definition, $\Delta\mathrm{SWE}_j$ is the difference between the SWE derived on time window j and the SWE derived on the previous time window $(j-1)$, i.e.

$$\Delta\mathrm{SWE}_j = \mathrm{SWE}(j) - \mathrm{SWE}(j-1) \tag{15}$$

As the densification for each $\Delta\mathrm{SWE}_j$ is considered separately, the density of a certain time step $\rho_{\mathrm{s},j}(n)$, which was added in time window j, and regarded at time step n is calculated by

$$\rho_{\mathrm{s},j}(n) = \rho_{\mathrm{s,new}} + \left(\rho_{\mathrm{s,d,\,max}} - \rho_{\mathrm{s,new}}\right)\left(1 - e^{-(n-j)/\tau}\right) \tag{16}$$

The density of a newly added $\Delta\mathrm{SWE}$ is set to be $\rho_{\mathrm{s,new}} = 100\ \mathrm{kg/m^3}$. This value can be assumed as the average density of freshly fallen dry snow in high-alpine regions, which is also used in several other model approaches (e.g., Lehning et al., 2002; López-Moreno et al., 2009; Schmid et al., 2014). In the course of time, the dry snow density exponentially approaches $\rho_{\mathrm{s,d,max}} = 357\ \mathrm{kg/m^3}$, being the average maximum dry snow density at the high-alpine study site Weissfluhjoch (Schmid et al., 2015). After $n = 30$ days, this value is reached with a deviation of 1% with $\tau = 6$, in case the time window is one day, and which was derived from HS and SWE recordings at the study site over several years. Figure S2b in the supporting information gives an example for the snow densification within an overall time span of 30 days. The density calculation is only defined for $n \geq j$. The thickness $\mathrm{D}_j(n)$ corresponding to $\Delta\mathrm{SWE}_j$ of time window j on time step n is

$$\mathrm{D}_j(n) = \begin{cases} \dfrac{\mathrm{SWE}_j}{\rho_{\mathrm{s,j}}(n)} & , n \geq j \\ 0 & , n < j. \end{cases} \tag{17}$$

The total thickness of the snowpack corresponds to HS and is the summed up for time step n

$$\mathrm{HS}(n) = \sum_{j=1}^{n} D_j(n) = \sum_{j=1}^{n} \frac{\mathrm{SWE}(j) - \mathrm{SWE}(j-1)}{\rho_{\mathrm{s,new}} + \left(\rho_{\mathrm{s,d,\,max}} - \rho_{\mathrm{s,new}}\right)\left(1 - e^{-(n-j)/\tau}\right)} \tag{18}$$

5. Processing Steps for Dry and Wet Snow

5.1. Processing Structure

The GPS signal processing is split into the determination of a snow-free reference and the calculation of snow cover properties for snow-covered periods (see Figure 3a).

5.2. Processing of Snow-Free Reference

We derived the baseline vector $\vec{b}_{12}$ with RTK positioning of GPS pseudorange and carrier phase measurements, and the signal strength reference $P_{\mathrm{m,ref}}$ during snow-free and clear sky conditions in autumn. As the coverage period of all 32 GPS satellite passing over the study site takes one sidereal day (~23 hr 56 min), we used reference data sets of full days with a raw data resolution of 1 s. To eliminate potential random atmospheric effects, we averaged six reference data sets with two corresponding data sets stemming from autumn dates in 2015, 2016, and 2017, before the three snow-covered seasons started. The differences in the baseline and the signal strength reference are negligible for the selected reference days. For the GPS setup at Weissfluhjoch, the baseline vector $\vec{b}_{12}$ pointing from GPS_1 to GPS_2, given in the ENU (East-North-Up) coordinate frame was

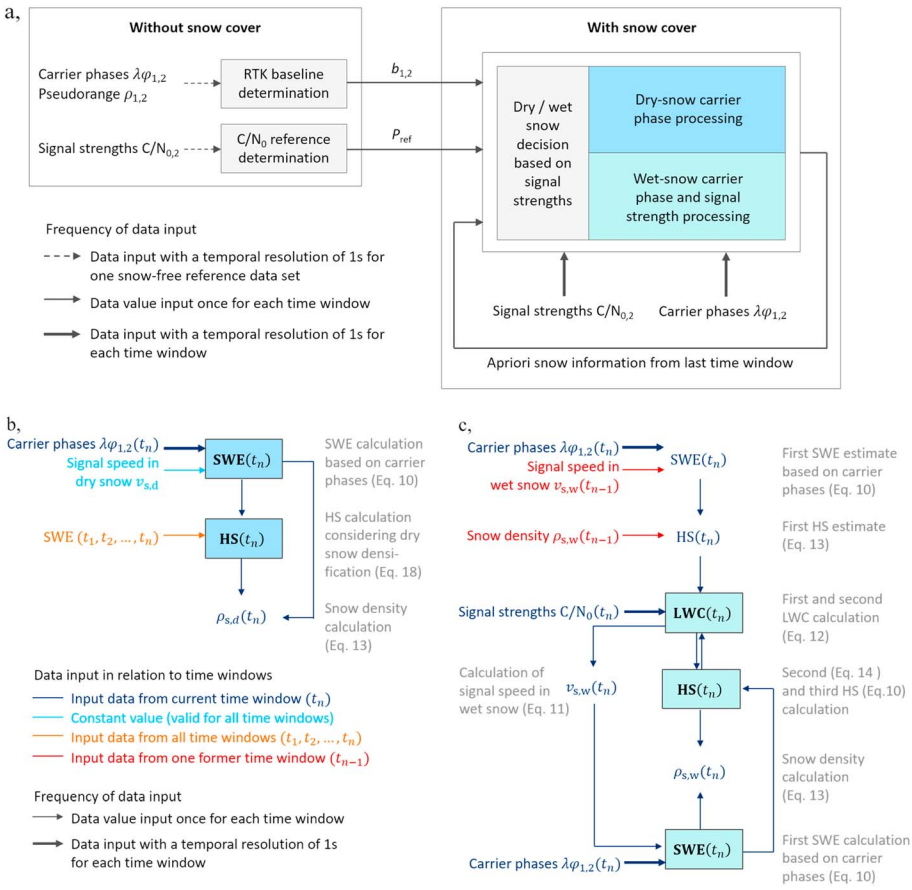

Figure 3. (a) Overview of the data input and processing structure of a snow-free reference determination and the determination of the snow cover properties for dry and wet snow. The numerical suffix 1 corresponds to data recorded at GPS_1, and 2 to GPS_2. (b) Overview of retrieval steps for the determination of snow water equivalent (SWE) and snow height (HS) for dry-snow conditions, and (c) SWE, HS, and liquid water content (LWC) for wet-snow conditions. Legend for c is shown in b.

$$\vec{b}_{12} = \begin{pmatrix} -1.781\ \text{m} \\ -3.961\ \text{m} \\ -4.992\ \text{m} \end{pmatrix}$$

The processed distance between GPS_1 and GPS_2 was determined to be 6.617 m with mm-accuracy. The baseline did not change during the entire study period. For the snow-free signal strength reference $P_{\text{m,ref}}$, we derived elevation-, azimuth- and GPS satellite-dependent classes during the entire reference time period. In addition, we calculated the average normalized signal strength over all classes for the snow-free reference period, which was 47.6 dB-Hz at GPS_2.

5.3. Processing Chains for Dry and Wet Snow

The raw GPS data input for the processing of time periods influenced by snow encompassed GPS carrier phase measurements and signal strength information and was 1 s. The raw data were processed for data sets of a time window of 24 hr to derive daily averages of SWE, HS, and LWC. The output included besides SWE and HS for dry snow also information on the snow density, and besides SWE, HS, and LWC for wet snow, additionally the density of wet snow and the speed of the signals in wet snow.

5.4. Dry/Wet Snow Decision

As a first step, the snow was classified based on signal strength information and $P_{\text{m,ref}}$ as either wet or dry (Figure 3a). For each time window, the class-dependent normalized signal strength $P_{\text{m,s}}$ was calculated as

described in section 4.2. Regarding all dry snow periods, the average normalized signal strength was 47.0 dB-Hz with a standard deviation of 0.6 dB-Hz. In average, it indicates a signal strength loss of approximately 0.6 dB-Hz compared to the snow-free reference. This decay confirms the findings of Koch et al. (2014) for previous years. However, as soon as the snow turns wet, the signal strength decreases exponentially, depending on the amount of snow and the LWC. Allowing a certain buffer, we set the dry/wet snow decision threshold to a signal strength loss of 1.2 dB-Hz. Related to the average signal strength for the snow-free reference periods, the threshold for the dry/wet snow decision was therefore at 46.4 dB-Hz. For signal strength values above this threshold, the snow was defined as dry and below this threshold as wet. As C/N_0 is a highly sensitive indicator, it is sufficient to rely on a few minutes of signal strength data to decide whether the entire data set should be further processed as 'dry' or 'wet' snow. However, as we consider entire 24-hr data sets, it is potentially possible that the wetting of snow occurs later in the data set. Therefore, we preprocessed the raw data for each 24-hr data set to derive normalized signal strength values of each 24-hr time window. Compared to the signal strength reference and applying the signal strength threshold, we defined for each 24-hr data set, if in the following processing step the snow should be considered as either dry or wet (see Figures 3b and 3c).

5.5. Processing of Dry Snow

The processing of dry snow is solely based on carrier phases as input and the assumption that the speed of signals in dry snow $v_{s,d}$ is constant. The two processing steps to derive SWE and HS are straightforward applying the carrier phase model for the SWE derivation (Eq. (10)) and the dry snow densification model solving for HS (Eq. (18)). The HS function relies on the evolution of each layer of the snowpack, using all previous SWE values from each past day as an input. In case HS is calculated incorrectly on a given day, it has no impact on the following day as it is not an input variable. Figure 3b shows the two processing steps we applied for dry snow. SWE, HS and the bulk snow density $\rho_{s,d}$ were stored as data outputs for each time window.

5.6. Processing of Wet Snow

For the wet snow retrieval, both signal strength and carrier phase measurements are needed as data inputs. The processing chain to derive SWE, HS, and LWC is more complex than for dry snow including two sequential iterative steps (see Figure 3c). The first part is similar to the processing in case of dry snow by applying the carrier phase model for the SWE derivation (Eq. (10)). As shown, the speed of signals in wet snow is not constant and depends on LWC, which was however not yet retrieved for the current time window. Therefore, we use the signal speed derived in the previous time step for the current time window as a first estimate. Even if it is not the correct signal speed for the current day, we can reasonably neglect this for the first estimate. The same assumption was made for the snow density to derive a first estimate of HS applying Eq. (13). In case of the first occurrence of wet snow after a dry snow period, the calculated dry snow density of the previous time period was used instead of $\rho_{s,w}$. With this first HS estimate and the GPS signal strength data of the current day, we derive LWC by using Eq. (12). As the signal strength is the dominant input variable for the LWC derivation, we can reasonably neglect the effect that the first HS estimate might be slightly biased in the direction of the previous day. As a next step, we recalculate HS applying Eq. (14) and in parallel also the signal speed in wet snow for the current day with Eq. (11). With this update, SWE, LWC, HS, and $\rho_{s,w}$, $v_{s,w}$ can be retrieved in a further processing round for the current time window. As further iterative rounds would only show a negligible change (less than 1%) in the derived snow cover properties, we restrict ourselves to only two iterations.

5.7. Transition Between Dry and Wet Snow

A high-alpine seasonal snowpack usually becomes wet at the beginning of spring due to increasing air temperature and solar radiation. Within our processing chain, this transition is covered. For the first time window representing wet snow, we start our first SWE and HS estimate with the signal speed of dry snow, which is then updated in the sequential iterative approach in the second processing round as shown above for the wet snow processing chain. Of course, a transition from wet to dry snow can occasionally occur. However, once the snowpack is completely wet, in a thick snowpack the water will rarely completely refreeze again and will also not completely drain as the so-called irreducible water content remains (Mitterer et al., 2011). For a shallow snowpack, however, the liquid water might refreeze again, leading to a decrease in

signal strength attenuation within the bulk snowpack, which is likely to occur at the beginning of a winter season in high alpine regions, but also during the entire season for sites at lower elevations.

6. Results and Discussion

The bulk snow cover properties SWE, HS, and LWC were derived continuously throughout the entire three winter seasons 2015-2016, 2016-2017, and 2017-2018 by applying the above proposed approach relying on GPS signal attenuation and time delay. In this section, we present and discuss the comparison of the GPS-derived snow cover properties with validation data measured in parallel at the study site Weissfluhjoch. Moreover, the precision of the processed GPS signals, which are the main input for the calculations of the snow cover properties, are evaluated. Finally, the advantages, limitations, and further enhancements are considered and discussed.

6.1. Comparison of GPS-Derived Seasonal Snowpack Evolution and Validation Data

Figure 4 presents the seasonal evolution of SWE, HS, and LWC derived by GPS and the continuous as well as manual snow pit validation data for the three winter seasons separately. The validation data for SWE encompasses snow pillow and snow scale data as well as two manual data sets (Manual 1 and 2) related to snow profile measurements as described in section 2.1. The validation data for HS include recordings from two ultrasonic sensors (Ultrasonic 1 and 2) as well as daily snow stake observation (Manual 3) and weekly to biweekly manual snow profile recordings (Manual 4). In addition, information on air and snow surface temperature, meltwater discharge recorded at a snow lysimeter and normalized GPS C/N_0 values are shown.

The snowpack evolution followed in each of the three winter seasons a typical high-alpine pattern of a snow-covered season from autumn to the beginning of summer. The onset of the continuous snow cover was between mid-October and early November. The melt-out date varied between mid-June and early July. According to Figure 4, the season with the deepest snowpack was 2017-2018, with maximum SWE values above 1,000 mm during several days, which were recorded at the snow pillow, the snow scale, and derived from the GPS signal. The SWE maximum in 2015-2016 and 2016-2017 was 850 and 750 mm, respectively. In addition to the high SWE values in 2018, of course, also, HS was higher compared the other two seasons with its maximum slightly above 3 m. The maximum HS values reached approximately 2 m in the other two seasons.

Each of the three winter seasons was divided into three periods, namely, the 'beginning of the snow-covered season' (cyan color shading), the 'dry-snow accumulation period' (without color shading), and the 'wet-snow melting period' (blue color shading). In the following, the main findings regarding the seasonal evolution of the GPS-derived snow cover properties as well as the validation data are summarized. A more detailed description is given in Text S1 in the supporting information. In Henkel et al. (2018), we already investigated the dry-snow accumulation period of the winter season 2015-2016.

In general, the GPS-derived snow cover properties followed the overall seasonal evolution very well. For SWE, the agreement between the different measurement methods was better during the dry-snow accumulation period than during the periods with wet snow. In all three seasons, occasional large deviations were obvious for the snow pillow and snow-scale measurements, which were most likely affected by bridging effects within the snowpack (Johnson & Marks, 2004). These measurement errors were especially prominent for both weighing devices at the end of April 2018 and for the snow scale also in the other two seasons. In addition, nonnatural heat-flux or drainage might lead to overestimations or underestimations (Johnson & Schaefer, 2002; Smith et al., 2017), which might be an issue especially at the beginning of the snow-covered season. In those times, snow pillow and snow scale were indeed not suited for validation. The GPS-derived SWE values seem then much more reliable and better fitted the manual SWE observations. In general, the manual measurements are considered to be reliable. Only the SWE Manual 1 and the HS Manuel 4 values were too high in spring 2018. The reason for this discrepancy was the uneven snow distribution within the study plot; HS was larger at the location where the snow profiles were taken at this time.

The seasonal evolution of HS was very similar for all measurement methods for all three seasons and during all periods. The applied snow densification approach allowed determining an increase in HS due to a snowfall with good accuracy. During the wet-snow melting period, the GPS-derived HS evolution was as well in good agreement with all other measurements; however, snowfall events were captured less precisely. During

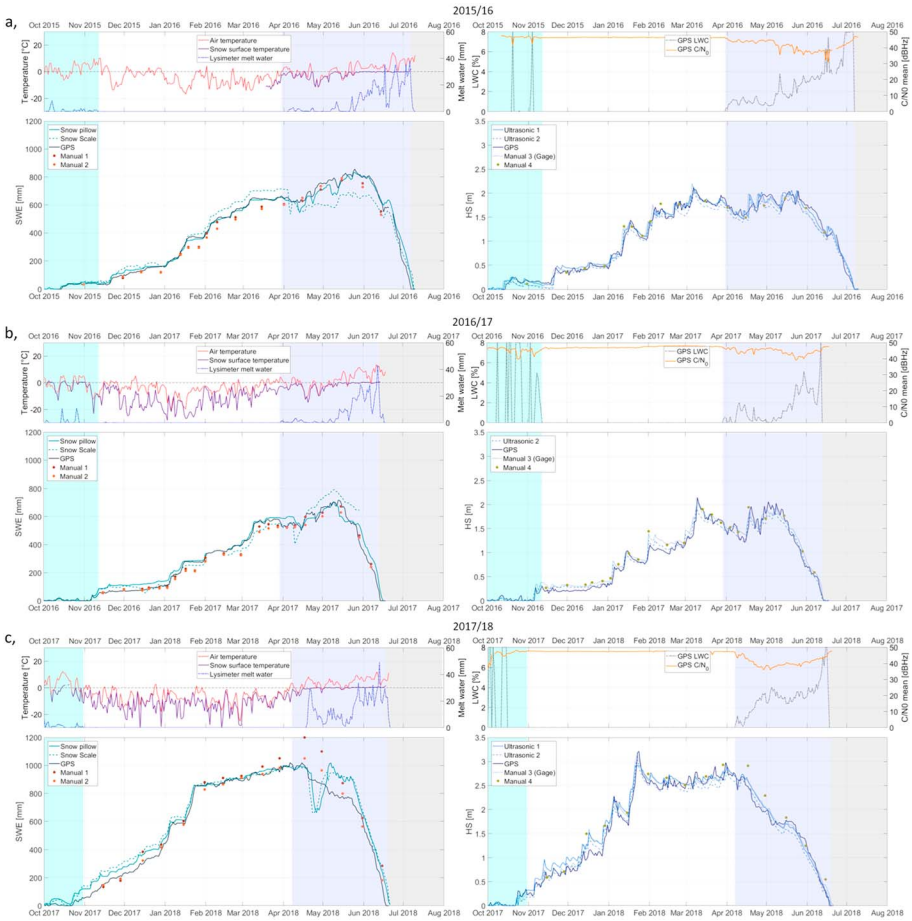

Figure 4. Global Positioning System (GPS)-derived snow water equivalent (SWE), snow height (HS), and liquid water content (LWC) and GPS C/N_0 in comparison to validation data at the Weissfluhjoch for the three winter seasons: (a) 2015-2016, (b) 2016-2017, and (c) 2017-2018. The cyan areas represent the periods at the beginning of the winter season with alternating dry- and wet-snow conditions, the white areas represent the dry-snow accumulation period, and the blue areas the wet-snow ablation period. The grey areas mark the snow-free time after ablation.

the entire dry-snow accumulation period, no melt-water outflow was recorded at the lysimeter. At the same time, the air and snow surface temperature were mainly below 0 °C. Regarding the evolution of melt-water in the melting period and on days with wet snow at the beginning of the snow-covered season, the occurrence and evolution of LWC were in line with the temperature evolution. However, as LWC and meltwater outflow describe different processes, they were not fully correlated, as, for example, the snowpack might contain liquid water without meltwater outflow yet. This was, for example, the case in spring 2018 when the meltwater outflow started approximately half a month later than the first occurrence of liquid water. As LWC is a volumetric measure and as HS is still low at the beginning of the snow-covered period, LWC easily reached high values of up to 8%. Moreover, in this period, the shallow snowpack was also likely to completely refreeze again. Within the wet-snow melting period, however, LWC changes are less quick and a certain irreducible water content remains at any time. In the melting period, LWC varied mainly between 1 and 4%; high values of LWC of up to 8% were only reached towards the melt-out date.

6.2. Statistical Comparison of All Measurements for Dry- and Wet-Snow Conditions

Figures 5a–5c show the results of the regression analysis comparing GPS-derived SWE and SWE measured at the snow pillow and the snow scale for the three winter seasons, separately for dry and wet snow. Each type of measurement was compared to the other ones. Besides the linear regression equation, also the root-mean-square error (RMSE) and the coefficient of determination (R^2) are given. The dry-snow values cover the

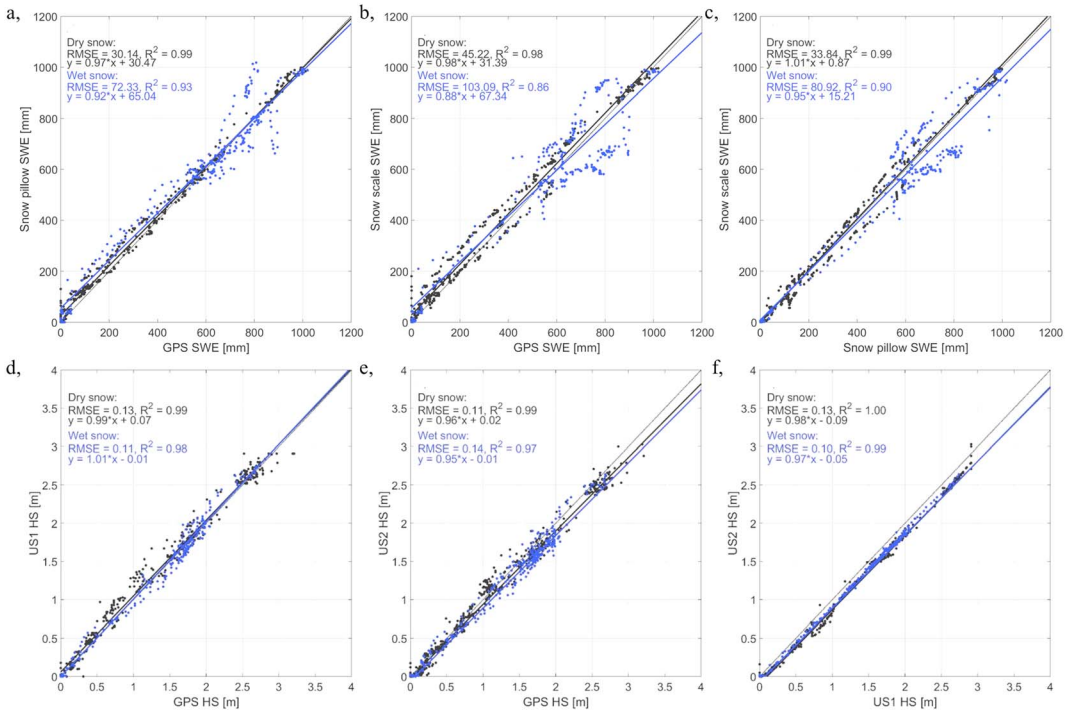

Figure 5. Global Positioning System (GPS)-derived versus measured validation data for snow water equivalent (SWE) and snow height (HS). Linear regression analysis, root-mean-square error (RMSE), and R^2 are given separately for dry- and wet-snow periods during all three seasons: a, (SWE): GPS versus snow pillow, (b) SWE: GPS versus snow scale, and (c) SWE: snow pillow versus snow scale. (d) HS: GPS versus US1, (e) GPS versus US2, and (f) US1 versus US2.

entire dry-snow accumulation period as well as dry snow days during the early season. The wet-snow values represent the entire wet-snow melting period as well as wet-snow days during the early season.

Overall, the agreement between GPS-derived, snow pillow and snow scale SWE values was very good. Comparing the results of the SWE regression analysis for dry- and wet-snow periods, the SWE values showed better agreement during dry-snow periods than during wet-snow periods for all methods. Deviations were particularly prominent in case of wet-snow conditions with SWE values above approximately 500 mm, when snow pillow, snow scale, and GPS differed more widely. The best fit was obtained for the comparison of GPS-derived values with snow pillow measurements both for dry- and wet-snow conditions (Figure 5a). Regarding dry snow, the RMSE and the R^2 were 30 mm and 0.99, respectively, for wet snow 72 mm and 0.93, respectively. The agreement of R^2 was about as good as, but slightly less for the RMSE, in the case of comparing snow pillow and snow scale (Figure 5c) with an RMSE of 34 mm for dry snow and 81 mm for wet snow. The regression results for the comparison of GPS-derived SWE and snow scale measurements were still good, but weaker than the other two comparisons with an RMSE of 45 mm for dry snow and 103 mm for wet snow (Figure 5b), which, however, mainly resulted from errors in the snow scale recordings due to bridging effects.

Figures 5d-5f show the results of the regression analysis comparing GPS-derived HS and HS measured with the Ultrasonic 1 and 2 sensors, each versus the other, for the three entire winter seasons. Results are again given separately for dry- and wet-snow conditions. As already mentioned, the HS values measured at Ultrasonic 1 were not available during the season 2016-2017. Comparing Figures 5a-5c and 5d-5f, the scatter was smaller for HS than for SWE, which might be due to the better accordance of the HS validation data in general. Regarding the results of the regression analyses in Figures 5d-5f, it is obvious that the correlation was highest for the two ultrasonic sensors (Figure 5f). Comparing the GPS-derived HS values with the measurements yielded a RMSE in the range of 0.10 to 0.14 m, similar to the range obtained for the ultrasonic measurements (0.10 to 0.13 m) and R^2 approached almost 1.0 in all cases. Moreover, for all comparisons the degree of agreement did not depend on the type of snow conditions: the fits were as good for dry- as for wet-snow conditions.

Table 1
Accuracy of GPS signal processing

Snow condition	SWE classes (mm)	n_{max}	μ_p (dB-Hz)	$RMSE_r$ (m)
No snow	0	10	47.72	0.009
Dry snow	250 (200-300)	9	46.95	0.009
	500 (450-550)	9	46.57	0.015
	750 (700-800)	8	47.59	0.024
	1,000 (950-1,050)	7	47.45	0.033
Wet snow, LWC: 2% (1.5-2.5%)	250 (200-300)	9	45.14	0.021
	500 (450-550)	8	43.35	0.029
	750 (700-800)	8	41.22	0.032
	1,000 (950-1,050)	7	41.53	0.052
Wet snow, LWC: 4% (3.5-4.5%)	250 (200-300)	9	43.48	0.026
	500 (450-550)	8	40.56	0.037
	750 (700-800)	7	37.83	0.042
Wet snow, LWC: 6% (5.5-6.5%)	250 (200-300)	6	42.41	0.027

Note. Average estimates for different SWE and LWC classes of the maximum possible number of satellites n_{max} above the elevation mask of 15°, which were simultaneously in view for processing, the mean normalized C/N_0 values, μ_p and the $RMSE_r$ comparing the DD carrier phase residuals r with fixed residual arcs. n_{max} and μ_p refer to the data recorded at GPS_2.
Abbreviations: DD, double difference; GPS, Global Positioning System; LWC, liquid water content; RMSE, root-mean-square error; SWE, snow water equivalent.

No direct LWC measurements were available for comparison during the three investigated winter seasons to validate the GPS-derived LWC values. However, for the winter seasons 2012-2013 and 2013-2014, Schmid et al. (2015) had compared continuous GPS-derived LWC values with LWC values derived by an upward-looking ground-penetrating radar (upGPR). Comparing GPS- and upGPR-derived LWC values for the range of 0 and 8% per volume, they reported an RMSE of 0.4 to 0.7 percent points indicating good agreement. We assume that the RMSE for the three winter seasons studied here were in a similar range since overall the characteristics of the winters did not differ much.

A more detailed analysis, including comparisons of all continuous and manual measurements, can be found in Text S2 and Tables S2, S3, and S4. In summary, the R^2 between the lysimeter meltwater outflow and the GPS-derived LWC values was 0.79 regarding all three seasons during the melting period in spring; R^2 was slightly lower (0.67) when also the wet snow periods in autumn were included. If all SWE validation data are compared to the GPS-derived results for all three winter seasons, the mean RMSE and R^2 were 41 mm and 0.99, respectively, for dry snow and 73 mm and 0.93, respectively, for wet snow, which is within the range if all SWE measurement methods are compared with each other. Regarding HS, RMSE and R^2 were 0.13 m and 0.98, respectively, for dry snow, and 0.14 m and 0.95, respectively, for wet snow.

6.3. Accuracy Analysis of GPS Signals

The GPS signals are the backbone of the snow cover property derivation. However, depending on the snow conditions, the signal quality and availability vary. Table 1 presents accuracy estimates of parameters for signal processing to compare no-snow, dry-snow, and wet-snow conditions; for wet-snow conditions different LWC values are considered. The summary statistics presented in Table 1 refer to a time window of 24 hr with a temporal resolution of the raw data of 1 s. Averages for the below given SWE and LWC classes include all days, which fall into a specific SWE or LWC class. For SWE, we selected five classes centered around 0, 250, 500, 750, and 1,000 mm each with a class width of ±50 mm, if snow was present, and for LWC four classes centered around 0, 2, 4, and 6% with a class width of ±0.5%, when liquid water was present. These classes cover a wide range of possible snow conditions. Only classes, which were covered in this study, are shown. For example, the classes of 4% LWC and 1,000 mm did not occur during the study period (Figure 4). Moreover, not all class were well populated, again reflecting the natural conditions. Nevertheless, Table 1 provides an overview on the signal accuracy estimations for typical conditions.

The table includes information on the maximum number of GPS satellites, which were simultaneously in view for the processing and information on the mean normalized C/N_0 values. In case of no snow, the maximum number of satellites was 10 for GPS_2. The satellite availability was slightly reduced with an

increase of SWE and LWC, which might be related to increasingly long pathways through the snowpack for signals with shallow angles. The signal strength was also highest during snow-free conditions and was slightly reduced during dry-snow conditions, but showing no correlation with the amount of snow. The class values lay in the range of the mean and standard deviation presented in section 5. The signal strength reduction from no snow to dry snow might mainly be caused by surface signal reflection (Koch et al., 2014; Steiner, Meindl, & Geiger, 2018) at the snow-air interface, which does not depend on the amount of snow. This interpretation is confirmed by the almost horizontal line of the normalized C/N_0, shown in Figure 4 in case of dry snow. However, as soon as the snow turns wet, the signal decreases more prominently, as can be seen for the classes of 1,000 and 750 mm with 2 and 4% LWC. This effect is mainly due to signal attenuation in wet snow (Koch et al., 2014). The values presented in the last column of Table 1 result from an RMSE analysis between DD carrier phase residuals and the fitted arcs as described in Henkel et al. (2018), which are also shown in S1 of the supporting information. Accuracy information on the carrier phase residuals is mainly representative for the SWE calculations. The $RMSE_r$ values indicate that the agreement between the residuals and the arcs decreases with an increase in SWE and LWC. SWE and LWC seem to contribute approximately to the same degree to an increase in $RMSE_r$ with values of 0.009 m for no snow and up to 0.052 m for 1,000 mm and 2% LWC. The decrease in accuracy is mainly caused by an increase in short-term phase multipath and phase noise. Nevertheless, it was still possible to derive all snow cover properties with sufficient accuracy as the long processing period of 24 hr allowed discarding potentially erroneous values. As this approach combines signal attenuation and time delay, the overall accuracy of all three GPS-derived snow cover parameters depends finally on both the normalized signal strength and the accuracy of the carrier phase residuals.

6.4. Advantages, Potential Limitations, and Further Enhancements

The proposed GPS snow monitoring approach has the prime advantage that three key bulk snow cover properties can simultaneously by derived with one sensor system only. This enables measuring SWE, HS, and LWC at the same location, which is usually not possible when applying different sensors for the different snow cover properties. Moreover, these low-cost GPS sensors are easy to install with a mast system and need rather little space regarding the small patch antennas with one installed below and a second one above the snow cover. Other sensors such as weighing sensors, radar systems, or snow lysimeters are up to 10 m^2 large, requiring more space on the ground including solid concrete foundations or caves in the ground, which make their installation difficult, man-power intense and expensive. As shown, the SWE pillow or scale measurements yield partly not consistent results and are burdened with problems such as bridging and errors due to nonnatural heat-fluxes, percolations, and drainages into the ground (Johnson & Marks, 2004; Johnson & Schaefer, 2002; Smith et al., 2017). Ongoing improvements to reduce the influence of edge stress concentrations at the weighing cells might lessen some of these problems in the future (Johnson et al., 2015). By using small low-cost GPS antennas, which can be directly placed on the ground of the area of investigation, the natural ground heat-flux is insignificantly affected. The presented GPS approach is nondestructive and can be applied continuously as it only relies on microwave electromagnetic waves travelling through the snowpack. This is especially an advantage compared to manual snow pit measurements as the latter are destructive, labor-intense, potentially subjective, and only provide a snapshot in time. With this GPS two-antenna approach, we consider the complex permittivity of the bulk snowpack. By using a multiantenna setup within the snowpack at different height levels, we may also detect permittivity changes within the snowpack.

The presented approach allows treating dry- and wet-snow conditions separately to adequately derive all snow cover properties by combining GPS signal time delay and GPS signal attenuation. This was so far not possible with previously presented GPS signal attenuation or GPS carrier phase-based methods. As demonstrated, it is possible to derive SWE, HS, and LWC even for a deep and wet snowpack. The maximum SWE, which was reached during our study period, was above 1,000 mm with up to 2% of LWC in April 2018. Even with a LWC of 4% and still rather high SWE values of about 800 mm later in spring 2018, all snow cover properties were derived successfully. We suppose that with our approach it is possible to cope with even larger SWE amounts for dry- and wet-snow conditions as the signals were still received in fair quality in late spring 2018. However, at one point the GPS signal processing might also become increasingly difficult if signal attenuation further increases. With a certain amount of snow and LWC, the signals might be attenuated

too strongly, causing too many interruptions in GPS signal tracking regarding the carrier phase measurements to correctly process the snow cover properties. As for dry snow the signal penetration depth within the L-band domain is orders of magnitude higher than for wet snow (Mätzler, 2002), further studies will focus on potential limitations for greater amounts of wet snow.

This approach can in general be used at any place on Earth, as the signals of all GNSS like GPS are freely available and ensure a global applicability even in remote and difficult to access regions, due to their orbital satellite constellation. However, deep valleys and steep slopes, especially when they are downhill oriented to the north on the northern hemisphere due to the orbital constellation, as well as coverages by objects such as trees and buildings in the direct surrounding are most probably limiting factors. For the estimation of the snow cover properties, carrier phase information of at least four satellites has to be received at both antennas. Regarding signal strength information, only one satellite would be sufficient, however, as this approach is a combined approach of signal strength and carrier phase information, the latter defines the minimum amount of four satellites as it is for standard positioning. Including further GNSS systems like Galileo, Glonass, and Beidou, the satellite coverage would increase, which would also improve the possibility to measure in difficult locations. A first step toward integration of Galileo was presented in Lamm et al. (2018) and will be further investigated in follow-up studies; for example, we intend to use this approach also for nonhorizontal terrain.

In this study, we present data at daily resolution, which is sufficient for many hydrological applications such as hydropower forecasts, and allows following the seasonal evolution. Of course, it would be possible to increase the temporal resolution, as presented with filtering options for SWE under dry-snow conditions by Henkel et al., 2018. Koch et al., 2014 provided subdaily LWC calculations showing subdaily melt-freeze cycles. For a stable derivation of carrier phase residuals and to compensate temporally specific satellite constellations, a period of at least 3 hr seems necessary. Applying, for example, moving window techniques as well as including other GNSS satellites besides GPS would definitely help to increase the temporal resolution, which is also subject of further investigations.

The presented approach and many of the previous studies have been performed at the high-alpine Weissfluhjoch study site. Some of the parameters used in the processing chain are site-specific. We suppose that our in situ measurements should also work at other locations, especially for sites with similar elevation and snow climate, but further investigations in other regions and at lower elevations are needed to corroborate the validity of the applied parameters. This is especially the case for the assumptions on the time-dependent densification to derive HS. To avoid potentially site-specific parameters, further developments could include a combination of deriving SWE and LWC with the approach presented and retrieving HS by GNSS reflectometry approaches (e.g., Larson et al., 2009). Moreover, at lower elevation sites rain-on-snow events with quickly varying dry- and wet-snow conditions may present a particular challenge, as they may cause rapid subdaily changes in snow density and LWC.

In fact, the presented approach was already successfully tested within the European Space Agency (ESA) business applications demo project SnowSense (2015-2018) at lower elevation sites, for example, at the Forêt Montmorency study site (673 m above sea level) in Quebec, Canada, as well as at several locations in Newfoundland, Canada (Appel et al., 2019). Based on the presented measurement algorithms and the described installation concept at the study site Weissfluhjoch, we furthermore developed self-supplied snow measurement stations including an integrated communication unit, which are ready to be used at further sites. To be applicable in remote and difficult to access areas, these measurement stations were designed to be easily transportable and contain a self-sufficient energy component with a solar panel and a battery, a mast system with rigging, an onboard processing unit, and a communication unit to transmit the processed data (Appel et al., 2017; Lamm et al., 2018). As this GPS approach represents a point-scale measurement, combining in situ data with remote sensing data and/or modeling methods should provide improved spatial information on SWE, HS, and LWC (Foppa et al., 2007; Magnusson et al., 2014; Pulliainen, 2006). Appel et al. (2019) recently presented promising results to improve hind- and forecast hydrological modeling as well as hydropower forecasts with such a combination. Moreover, such in situ measurements have the potential for serving as valuable ground truth for various remote sensing and modeling approaches for dry-snow and the even more challenging wet-snow conditions, for example, for microwave remote sensing approaches.

7. Conclusions

We presented a novel approach to simultaneously derive with a single sensor system the snow cover properties SWE, HS, and snow LWC based on a combination of GPS signal attenuation and time delay. To this end, we applied a low-cost GPS sensor setup consisting of two antennas. One antenna was installed on the ground level, remaining below the snowpack during the snow-covered periods. The other antenna was mounted on a pole, being permanently above the snow cover. The GPS sensor system was installed and operated at the high-alpine study site Weissfluhjoch in Switzerland for three entire winter seasons between autumn 2015 and summer 2018. Our GPS approach allows deriving the three snow cover properties simultaneously and nondestructively for dry- and wet-snow conditions based on microwave signals travelling through the snowpack. It relies on the interaction of signals with dielectric properties, which differs largely between snow-free, dry-snow and wet-snow conditions. The processing of snow-covered periods is handled differently for dry- and wet-snow conditions. We considered signal time delay and attenuation including reflection and refraction processes using a combination of GPS carrier phases and GPS signal strength information; the latter expressed as the signal-to-noise power density ratio C/N_0, to jointly derive SWE, HS, and LWC.

The GPS-derived SWE, HS, and LWC values showed a high degree of agreement with validation data recorded in parallel at the study site for the three entire winter seasons. The GPS-derived LWC showed a good accordance with the melt-water outflow at a snow lysimeter. Regarding SWE, the agreement of all validation data compared to the GPS results was slightly higher for dry snow conditions (RMSE: 41 mm, R^2: 0.99) than for wet snow conditions (RMSE: 73 mm, R^2: 0.93), which is conform to the overall agreement of all SWE measurement methods. The best agreement was found between GPS and snow pillow data. Regarding HS, the agreement between all methods is even better. Comparing the GPS-derived HS results with the validation data, the agreement for dry snow (RMSE: 0.13 m, R^2: 0.98) and wet snow (RMSE: 0.14 m, R^2: 0.95) is very good. Even for a deep snowpack with SWE above 1,000 mm and HS slightly above 3 m, the snow cover properties were reliably derived under dry- and wet-snow conditions. The accuracy of the GPS signal approach was estimated for different SWE and LWC classes and showed that the snow parameters can be consistently determined for a wide range of snow conditions. Further validation will be needed to confirm the applicability of the presented approach at lower elevation sites with more variable snow conditions. As we use low-cost GPS sensor components, sensor networks become feasible, which offer a better spatial and temporal coverage. As shown within the SnowSense project (Appel et al., 2019), the in situ data can be assimilated into modeling or remote sensing snow products to, for example, improve the prediction of melt water runoff and hydropower forecasts for large catchments. Moreover, buried GPS sensors in slopes may support snow management in ski resort or local avalanche forecasting.

Acknowledgments

F. Koch, P. Henkel, F. Appel, and M. Lamm were co-funded by the European Space Agency (ESA, 000113149/14/NL/AD) within the ESA business applications demo project SnowSense (2015-2018; https://business.esa.int/projects/snowsense-dp), which is gratefully acknowledged. Many thanks to Christoph Marty for valuable discussions on SWE and HS measurements. We thank all SLF staff members, who performed manual snow measurements and snow pit observations. The data that support and underlie the conclusions of this manuscript are available on the EnviDat platform (https://doi.org/10.16904/envidat.56; https://www.envidat.ch).

References

Appel, F., Henkel, P., Koch, F., Mauser, W. (2017). Vorrichtung zur Bestimmung von Schneeparametern. Publication of German Patent Application, appl. Nr.: DE 10 2017 110 992 A1 2017.12.28, appl. date: 19.05.2017.

Appel, F., Koch, F., Rösel, A., Klug, P., Henkel, P., Lamm, M., et al. (2019). Advances in snow hydrology using a combined approach of GNSS in situ stations, hydrological modelling and Earth observation—A case study in Canada. *Geosciences*, *9*(1), 44. https://doi.org/10.3390/geosciences9010044

Avanzi, F., Caruso, M., Jommi, C., De Michele, C., & Ghezzi, A. (2014). Continuous-time monitoring of liquid water content in snowpacks using capacitance probes: A preliminary feasibility study. *Advances in Water Resources*, *68*, 32–41. https://doi.org/10.1016/j.advwatres.2014.02.012

Beaumont, R. T. (1966). *Evaluation of the Mt. Hood pressure pillow snow gage and application to forecasting avalanche hazard* (Vol. 69, pp. 341–349). IAHS Publications.

Bernhardt, M., Schulz, K., Liston, G. E., & Zängl, C. (2012). The influence of lateral snow redistribution processes on snow melt and sublimation in alpine regions. *Journal of Hydrology*, *424*, 196–206.

Boniface, K., Braun, J. J., McCreight, J. L., & Nievinski, F. G. (2015). Comparison of snow data assimilation system with GPS reflectometry snow depth in the western United States. *Hydrological Processes*, *29*(10), 2425–2437. https://doi.org/10.1002/hyp.10346

Bormann, K. J., Westra, S., Evans, J. P., & McCabe, M. F. (2013). Spatial and temporal variability in seasonal snow density. *Journal of Hydrology*, *484*, 63–73. https://doi.org/10.1016/j.jhydrol.2013.01.032

Botteron, C., Dawes, N., Leclère, J., Skaloud, J., Weijs, S. V., & Farine, P. A. (2013). Soil moisture & snow properties determination with GNSS in alpine environments: Challenges, status, and perspectives. *Remote Sensing*, *5*(7), 3516–3543. https://doi.org/10.3390/rs5073516

Boyne, H. S., & Fisk, D. (1987). A comparison of snow cover liquid water measurement techniques. *Water Resources Research*, *23*(10), 1833–1836. https://doi.org/10.1029/WR023i010p01833

Bradford, J. H., Harper, J. T., & Brown, J. (2009). Complex dielectric permittivity measurements from ground-penetrating radar data to estimate snow liquid water content in the pendular regime. *Water Resources Research*, *45*, W08403. https://doi.org/10.1029/2008WR007341

Bühler, Y., Adams, M. S., Bösch, R., & Stoffel, A. (2016). Mapping snow depth in alpine terrain with unmanned aerial systems (UASs): Potential and limitations. *The Cryosphere*, *10*(3), 1075–1088. https://doi.org/10.5194/tc-10-1075-2016

Cardellach, E., Fabra, F., Nogués-Correig, O., Oliveras, S., Ribó, S., & Rius, A. (2011). GNSS-R ground-based and airborne campaigns for ocean, land, ice, and snow techniques: Application to the GOLD-RTR data sets. *Radio Science*, *46*, RS0C04. https://doi.org/10.1029/2011RS004683

Denoth, A. (1989). Snow dielectric measurements. *Advances in Space Research*, *9*(1), 233–243. https://doi.org/10.1016/0273-1177(89)90491-2

Dietz, A. J., Kuenzer, C., Gessner, U., & Dech, S. (2012). Remote sensing of snow—A review of available methods. *International Journal of Remote Sensing*, *33*(13), 4094–4134. https://doi.org/10.1080/01431161.2011.640964

Fierz, C., Armstrong, R.L., Durand, Y., Etchevers, P., Greene, E., McClung, D. M., et al. (2009). The international classification for seasonal snow on the ground, In: UNESCO-IHP, Tech. Rep., 25, Paris, France.

Foppa, N., Stoffel, A., & Meister, R. (2007). Synergy of in situ and space borne observation for snow depth mapping in the Swiss Alps. *International Journal of Applied Earth Observation and Geoinformation*, *9*(3), 294–310. https://doi.org/10.1016/j.jag.2006.10.001

Frey, S., & Holzman, H. (2015). A conceptual, distributed snow redistribution model. *Hydrology and Earth System Sciences*, *19*(11), 4517–4530. https://doi.org/10.5194/hess-19-4517-2015

Goodison, B. E., Glynn, J. E., Harvey, K. D., & Slater, J. E. (1987). Snow surveying in Canada: A perspective. *Canadian Water Resources Journal*, *12*(2), 27–42. https://doi.org/10.4296/cwrj1202027

Grünewald, T., Schirmer, M., Mott, R., & Lehning, M. (2010). Spatial and temporal variability of snow depth and SWE in a small mountain catchment. *The Cryosphere*, *4*(2), 215–225. https://doi.org/10.5194/tc-4-215-2010

Gutmann, E. D., Larson, K. M., Williams, M. W., Nievinski, F. G., & Zavorotny, V. (2012). Snow measurement by GPS interferometric reflectometry: An evaluation at Niwot Ridge, Colorado. *Hydrological Processes*, *26*(19), 2951–2961. https://doi.org/10.1002/hyp.8329

Hall, D. (2012). *Remote sensing of ice and snow*. Springer.

Härer, S., Bernhardt, M., Siebers, M., & Schulz, K. (2018). On the need for a time- and location-dependent estimation of the NDSI threshold value for reducing existing uncertainties in snow cover maps at different scales. *The Cryosphere*, *12*(5), 1629–1642. https://doi.org/10.5194/tc-12-1629-2018

Heilig, A., Mitterer, C., Schmid, L., Wever, N., Schweizer, J., Marshall, H. P., & Eisen, O. (2015). Seasonal and diurnal cycles of liquid water in snow—Measurements and modelling. *Journal of Geophysical Research: Earth Surface*, *120*, 2139–2154. https://doi.org/10.1002/2015JF003593

Henkel, P. & Cárdenas, J. (2014). Method for determining a baseline between two receivers. European Patent 2 749 900 A1, Jul. 2, 2014.

Henkel, P., Koch, F., Appel, F., Bach, H., Prasch, M., Schmid, L., et al. (2018). Snow water equivalent of dry snow derived from GNSS Carrier Phases. *IEEE Transactions on Geoscience and Remote Sensing*, *56*(6), 3561–3572. https://doi.org/10.1109/TGRS.2018.2802494

Henkel, P., Koch, F., Appel, F., Mauser, W. (2017). Verfahren zur Bestimmung von Schneeparametern. Publication of German Patent Application, appl. Nr.: DE 10 2017 110 994 A1 2017.12.28, appl. date: 19.05.2017.

Henkel, P., Mittmann, U. & Iafrancesco, M. (2016). Real-time kinematic positioning with GPS and GLONASS. Proc. 24th Eur. Signal Process. Conf. (EUSIPCO), Budapest, Hungary, Aug./Sep. 2016, pp. 1063–1067.

Hofmann-Wellenhof, B., Lichtenegger, H., & Wasle, E. (2007). *GNSS–global navigation satellite systems: GPS, GLONASS, Galileo, and more*. Springer.

Immerzeel, W. W., Droogers, P., De Jong, S., & Bierkens, M. (2009). Large-scale monitoring of snow cover and runoff simulation in Himalayan river basins using remote sensing. *Remote Sensing of Environment*, *113*(1), 40–49. https://doi.org/10.1016/j.rse.2008.08.010

Jin, S., Cardellach, E., & Xie, F. (2014). *GNSS Remote Sensing*. Springer. https://doi.org/10.1007/978-94-007-7482-7

Johnson, J., Gelvin, A., Duvoy, P., Schaefer, G., Poole, G., & Horton, G. (2015). Performance characteristics of a new electronic snow water equivalent sensor in different climates. *Hydrological Processes*, *29*(6), 1418–1433. https://doi.org/10.1002/hyp.10211

Johnson, J. B., & Marks, D. (2004). The detection and correction of snow water equivalent pressure sensor errors. *Hydrological Processes*, *18*(18), 3513–3525.

Johnson, J. B., & Schaefer, G. L. (2002). The influence of thermal, hydrologic and snow deformation mechanics on snow water equivalent pressure sensor accuracy. *Hydrological Processes*, *16*(18), 3529–3542. https://doi.org/10.1002/hyp.1236

Jonas, T., Marty, C., & Magnusson, J. (2009). Estimating the snow water equivalent from snow depth measurements in the Swiss Alps. *Journal of Hydrology*, *378*(1-2), 161–167. https://doi.org/10.1016/j.jhydrol.2009.09.021

Kim, E., Gatabe, C., Hall, D., Newlin, J., Misakonis, A., Elder, K., et al. (2017). Overview of SnowEx Year 1 Activities. Available online: https://ntrs.nasa.gov/search.jsp? R=20170007518.

Kinar, N., & Pomeroy, J. (2015). Measurements of the physical properties of the snowpack. *Reviews of Geophysics*, *53*, 481–544. https://doi.org/10.1002/2015RG000481

Koch, F. (2017). Snow cover properties and soil moisture derived from GPS signals (Doctoral dissertation). Retrieved from Electronic Thesis of LMU Munich. (https://edoc.ub.uni-muenchen.de/21938/). Munich, Germany: Ludwig-Maximilians-Universität München.

Koch, F., Prasch, M., Schmid, L., Schweizer, J., & Mauser, W. (2014). Measuring snow liquid water content with low-cost GPS receivers. *Sensors*, *14*(11), 20975–20999. https://doi.org/10.3390/s141120975

Koch, F., Schlenz, F., Prasch, M., Appel, F., Ruf, T., & Mauser, W. (2016). Soil moisture retrieval based on GPS signal strength attenuation. *Water*, *8*(7), 276. https://doi.org/10.3390/w8070276

Lamm, M., Koch, F., Appel. F., & Henkel, P. (2018). Estimation of snow parameters with GPS and Galileo. Proc. of the IEEE 60-th International Symposium ELMAR, Zadar, Croatia, 16.-19. Sep. 2018.

Larson, K., Gutmann, E., Zavorotny, V., Braun, J., Williams, M., & Nievinski, F. (2009). Can we measure snow depth with GPS receivers? *Geophysical Research Letters*, *36*, L17502. https://doi.org/10.1029/2009GL039430

Larson, K. M. (2016). GPS interferometric reflectometry: Applications to surface soil moisture, snow depth, and vegetation water content in the western United States. *Wiley Interdisciplinary Reviews: Water*, *3*(6), 775–787. https://doi.org/10.1002/wat2.1167

Lehning, M., Bartelt, P., Brown, B., & Fierz, C. (2002). A physical SNOWPACK model for the Swiss avalanche warning: Part III: Meteorological forcing, thin layer formation and evaluation. *Cold Regions Science and Technology*, *35*(3), 169–184. https://doi.org/10.1016/S0165-232X(02)00072-1

Lighari, R. U. R., Berg, M., Salonen, E. T., & Parssinen, A. (2017). Classification of GNSS SNR data for different environments and satellite orbital information. 11th European Conference on Antennas and Propagation (EUCAP), IEEE, 2088-2092.

López-Moreno, J. I., Goyette, S., & Beniston, M. (2009). Impact of climate change on snowpack in the Pyrenees: Horizontal spatial variability and vertical gradients. *Journal of Hydrology*, *374*(3-4), 384–396. https://doi.org/10.1016/j.jhydrol.2009.06.049

Lundberg, A., Granlund, N., & Gustafsson, D. (2010). Towards automated 'Ground truth'snow measurements—A review of operational and new measurement methods for Sweden, Norway, and Finland. *Hydrological Processes*, *24*(14), 1955–1970.
Lundberg, A., & Thunehed, H. (2000). Snow wetness influence on impulse radar snow surveys theoretical and laboratory study. *Nordic Hydrology*, *31*(2), 89–106. https://doi.org/10.2166/nh.2000.0007
Magnusson, J., Gustafsson, D., Husler, F., & Jonas, T. (2014). Assimilation of point SWE data into a distributed snow cover model comparing two contrasting methods. *Water Resources Research*, *50*, 7816–7835. https://doi.org/10.1002/2014WR015302
Mankin, J. S., Viviroli, D., Singh, D., Hoekstra, A. Y., & Diffenbaugh, N. S. (2015). The potential for snow to supply human water demand in the present and future. *Environmental Research Letters*, *10*(11), 114016. https://doi.org/10.1088/1748-9326/10/11/114016
Marty, C. (2017). GCOS SWE data from 11 stations in Switzerland; WSL Institute for Snow and Avalanche Research SLF, Tech. Rep., WSL Institute for Snow and Avalanche Research SLF, Davos, Switzerland. https://doi.org/10.16904/15
Marty, C., & Meister, R. (2012). Long-term snow and weather observations at Weissfluhjoch and its relation to other high-altitude observatories in the Alps. *Theoretical and Applied Climatology*, *110*(4), 573–583. https://doi.org/10.1007/s00704-012-0584-3
Mätzler, C. (2002). COST Action 712: Microwave radiometry. In F. S. Marzano & G. Visconti (Eds.), *Remote Sensing of Atmosphere and Ocean from Space: Models, Instruments and Techniques* (pp. 231–246). Springer.
Mauser, W., & Prasch, M. (2015). *Regional assessment of global change impacts: The Project GLOWA-Danube*. Springer.
McCreight, J. L., Small, E. E., & Larson, K. M. (2014). Snow depth, density, and SWE estimates derived from GPS reflection data: Validation in the western US. *Water Resources Research*, *50*, 6892–6909. https://doi.org/10.1002/2014WR015561
Mitterer, C., Heilig, A., Schweizer, J., & Eisen, O. (2011). Upward-looking ground-penetrating radar for measuring wet-snow properties. *Cold Regions Science and Technology*, *69*, 129–138.
Nagler, T., Rott, H., Ripper, E., Bippus, G., & Hetzenecker, M. (2016). Advancements for snowmelt monitoring by means of Sentinel-1 SAR. *Remote Sensing*, *8*(4), 348. https://doi.org/10.3390/rs8040348
Parajka, J., & Blöschl, G. (2006). Validation of MODIS snow cover images over Austria. *Hydrology and Earth System Sciences*, *10*(5), 679–689. https://doi.org/10.5194/hess-10-679-2006
Pirazzini, R., Leppaenen, L., Picard, G., Lopez-Moreno, J. I., Marty, C., Macelloni, M., et al. (2018). European in-situ snow measurements: Practices and purposes. *Sensors*, *18*(7). https://doi.org/10.3390/s18072016
Pomeroy, J., Bernhardt, M., & Marks, D. (2015). Water resources: Research network to track alpine water. *Nature*, *521*(7550), 32. https://doi.org/10.1038/521032c
Prokop, A. (2008). Assessing the applicability of terrestrial laser scanning for spatial snow depth measurements. *Cold Regions Science and Technology*, *54*(3), 155–163. https://doi.org/10.1016/j.coldregions.2008.07.002
Pulliainen, J. (2006). Mapping snow water equivalent and snow depth in boreal and sub-arctic zones by assimilating space-borne microwave radiometer data and ground-based observations. *Remote Sensing of Environment*, *101*(2), 257–269. https://doi.org/10.1016/j.rse.2006.01.002
Raleigh, M. S., & Lundquist, J. D. (2012). Comparing and combining SWE estimates from the SNOW-17 model using PRISM and SWE reconstruction. *Water Resources Research*, *48*, W01506. https://doi.org/10.1029/2011WR010542
Roth, K., Schulin, R., Flühler, H., & Attinger, W. (1990). Calibration of time domain reflectometry for water-content measurement using a composite dielectric approach. *Water Resources Research*, *26*(10), 2267–2273.
Schattan, P., Baroni, G., Oswald, S. E., Schober, J., Frey, C., Kormann, C., et al. (2017). Continuous monitoring of snowpack dynamics in alpine terrain by aboveground neutron sensing. *Water Resources Research*, *53*, 3615–3634. https://doi.org/10.1002/2016WR020234
Schleppe, J., & Lachapelle, G. (2008). Tracking performance of a HSGPS receiver under avalanche deposited snow. *GPS Solutions*, *12*(1), 13–21. https://doi.org/10.1007/s10291-007-0060-1
Schmid, L., Heilig, A., Mitterer, C., Schweizer, J., Maurer, H., Okorn, R., & Eisen, O. (2014). Continuous snowpack monitoring using upward-looking ground-penetrating radar technology. *Journal of Glaciology*, *60*(221), 509–525. https://doi.org/10.3189/2014JoG13J084
Schmid, L., Koch, F., Heilig, A., Prasch, M., Eisen, O., Mauser, W., & Schweizer, J. (2015). A novel sensor combination (upGPR–GPS) to continuously and non-destructively derive snow cover properties. *Geophysical Research Letters*, *42*, 3397–3405. https://doi.org/10.1002/2015GL063732
Schneebeli, M., Coléou, C., Touvier, F., & Lesaffre, B. (1998). Measurement of density and wetness in snow using time-domain reflectometry. *Annals of Glaciology*, *26*, 69–72. https://doi.org/10.1017/S0260305500014580
Sigouin, M. J., & Si, B. C. (2016). Calibration of a non-invasive cosmic-ray probe for wide area snow water equivalent measurement. *The Cryosphere*, *10*(3), 1181–1190. https://doi.org/10.5194/tc-10-1181-2016
Sihvola, A., & Tiuri, M. (1986). Snow fork for field determination of the density and wetness profiles of a snow pack. *IEEE Transactions on Geoscience and Remote Sensing*, *24*(5), 717–721.
Smith, C., Kontu, A., Laffin, R., & Pommeroy, J. (2017). An assessment of two automated snow water equivalent instruments during the WMO Solid Precipitation Intercomparison Experiment. *The Cryosphere*, *11*(1), 101–116. https://doi.org/10.5194/tc-11-101-2017
Steiner, L., Meindl, M., Fierz, C., & Geiger, A. (2018). An assessment of sub-snow GPS for quantification of snow water equivalent. *The Cryosphere*, *12*(10), 3161–3175. https://doi.org/10.5194/tc-12-3161-2018
Steiner, L., Meindl, M., & Geiger, A. (2018). Characteristics and limitations of GPS L1 observations from submerged antennas. *Journal of Geodesy*, *93*(2), 267–280. https://doi.org/10.1007/s00190-018-1147-x
Stepanek, J., & Claypool, D. W. (1997). GPS signal reception under snow cover: A pilot study establishing the potential usefulness of GPS in avalanche search and rescue operations. *Wilderness and Environmental Medicine*, *8*(2), 101–104. https://doi.org/10.1580/1080-6032(1997)008[0101:GSRUSC]2.3.CO;2
Sturm, M. (2015). White water: Fifty years of snow research in WRR and the outlook for the future. *Water Resources Research*, *51*, 4948–4965. https://doi.org/10.1002/2015WR017242
Sturm, M., Taras, B., Liston, G. E., Derksen, C., Jonas, T., & Lea, J. (2010). Estimating snow water equivalent using snow depth data and climate classes. *Journal of Hydrometeorology*, *11*(6), 1380–1394. https://doi.org/10.1175/2010JHM1202.1
Takala, M., Luojus, K., Pulliainen, J., Derksen, C., Lemmetyinen, J., Kärnä, J. P., et al. (2011). Estimating northern hemisphere snow water equivalent for climate research through assimilation of space-borne radiometer data and ground-based measurements. *Remote Sensing of Environment*, *115*(12), 3517–3529. https://doi.org/10.1016/j.rse.2011.08.014
Talbot, N. C. (1993). Centimeters in the field, a users perspective of real-time kinematic positioning in a production environment. *Proc. 6th Int. Tech. Meeting Satellite Division Inst. Navigat. (ION GPS)*, Salt Lake City, UT, USA, 1049-1057.
Techel, F., & Pielmeier, C. (2011). Point observations of liquid water content in wet snow-investigating methodical, spatial and temporal aspects. *The Cryosphere*, *5*(2), 405–418. https://doi.org/10.5194/tc-5-405-2011

Tedesco, M. (2014). *Remote Sensing of the Cryosphere*. Wiley.
Teunissen, P. J. G. (1995a). *On the GPS double-difference ambiguities and their partial search spaces. Geodetic Theory Today* (pp. 39–48). Springer. https://doi.org/10.1007/978-3-642-79824-5_10
Teunissen, P. J. G. (1995b). The least-squares ambiguity decorrelation adjustment: A method for fast GPS integer ambiguity estimation. *Journal of Geodesy*, *70*(1-2), 65–82. https://doi.org/10.1007/BF00863419
Tiuri, M., Sihvola, A., Nyfors, E., & Hallikainen, M. (1984). The complex dielectric constant of snow at microwave frequencies. *IEEE Journal of Oceanic Engineering*, *9*(5), 377–382. https://doi.org/10.1109/JOE.1984.1145645
Ulaby, F. T., Long, D. G., Blackwell, W. J., Elachi, C., Fung, A. K., Ruf, C., et al. (2014). *Microwave radar and radiometric remote sensing. The University of.* Michigan Press.
Vey, S., Güntner, A., Wickert, J., Blume, T., Thoss, H., & Ramatschi, M. (2016). Monitoring snow depth by GNSS Reflectometry in built-up areas: A case study for Wettzell, Germany. *IEEE Journal of selected topics in applied Earth observations and Remote Sensing*, *9*(10), 4809–4816. https://doi.org/10.1109/JSTARS.2016.2516041
Vionnet, V., Brun, E., Morin, S., Boone, A., Faroux, S., LeMoigne, P., et al. (2012). The detailed snowpack scheme Crocus and its implementation in SURFEX v7.2. *Geoscientific Model Development*, *5*, 773–791.
Viviroli, D., Dürr, H. H., Messerli, B., Meybeck, M., & Weingartner, R. (2007). Mountains of the world, water towers for humanity: Typology, mapping, and global significance. *Water resources research*, *43*, W07447. https://doi.org/10.1029/2006WR005653
Warscher, M., Strasser, U., Kraller, G., Marke, T., Franz, H., & Kunstmann, H. (2013). Performance of complex snow cover descriptions in a distributed hydrological model system: A case study for the high Alpine terrain of the Berchtesgaden Alps. *Water resources research*, *49*, 2619–2637. https://doi.org/10.1002/wrcr.20219
Weber, M., Bernhardt, M., Pomeroy, J. W., Fang, X., Härer, S., & Schulz, K. (2016). Description of current and future snow processes in a small basin in the Bavarian Alps. *Environmental Earth Sciences*, *75*(17), 1223. https://doi.org/10.1007/s12665-016-6027-1
Wesemann, J., Herrnegger, M., & Schulz, K. (2018). Hydrological modelling in the anthroposphere: Predicting local runoff in a heavily modified high-alpine catchment. *Journal of Mountain Science*, *15*(5), 921–938. https://doi.org/10.1007/s11629-017-4587-5
Woodhouse, I. H. (2005). *Introduction to Microwave Remote Sensing*. Taylor & Francis.
World Meteorological Organization (2018). Essential Climate Variables. https://public.wmo.int/en/programmes/global-climate-observing-system/essential-climate-variables (accessed online: 20 October 2018).